UCSF
UC San Francisco Previously Published Works

Title
Top-down control of hippocampal signal-to-noise by prefrontal long-range inhibition

Permalink
https://escholarship.org/uc/item/7rh962bk

Journal
Cell, 185(9)

ISSN
0092-8674

Authors
Malik, Ruchi
Li, Yi
Schamiloglu, Selin
et al.

Publication Date
2022-04-01

DOI
10.1016/j.cell.2022.04.001

Peer reviewed

eScholarship.org Powered by the California Digital Library
University of California

Author Manuscript

Author Manuscript

Author Manuscript

Author Manuscript

HHS Public Access

Author manuscript

Cell. Author manuscript; available in PMC 2023 March 20.

Published in final edited form as:

Cell. 2022 April 28; 185(9): 1602–1617.e17. doi:10.1016/j.cell.2022.04.001.

Top-down control of hippocampal signal-to-noise by prefrontal long-range inhibition

Ruchi Malik[1], **Yi Li**[1], **Selin Schamiloglu**[1], **Vikaas S. Sohal**[1,2,*]

[1]Department of Psychiatry and Behavioral Sciences, UCSF Weill Institute for Neurosciences, Kavli Institute for Fundamental Neuroscience, University of California San Francisco, San Francisco, CA, USA

[2]Lead contact

SUMMARY

Prefrontal cortex (PFC) is postulated to exert "top-down control" on information processing throughout the brain to promote specific behaviors. However, pathways mediating top-down control remain poorly understood. In particular, knowledge about direct prefrontal connections that might facilitate top-down control of hippocampal information processing remains sparse. Here we describe monosynaptic long-range GABAergic projections from PFC to hippocampus. These preferentially inhibit vasoactive intestinal polypeptide-expressing interneurons, which are known to disinhibit hippocampal microcircuits. Indeed, stimulating prefrontal–hippocampal GABAergic projections increases hippocampal feedforward inhibition and reduces hippocampal activity *in vivo*. The net effect of these actions is to specifically enhance the signal-to-noise ratio for hippocampal encoding of object locations and augment object-induced increases in spatial information. Correspondingly, activating or inhibiting these projections promotes or suppresses object exploration, respectively. Together, these results elucidate a top-down prefrontal pathway in which long-range GABAergic projections target disinhibitory microcircuits, thereby enhancing signals and network dynamics underlying exploratory behavior.

In brief

Long-range GABAergic projections from the prefrontal cortex to dorsal hippocampus are identified, which modulate spatial encoding, CA1-PFC gamma synchrony, and object exploration.

Graphical Abstract

*Correspondence: vikaas.sohal@ucsf.edu.

AUTHOR CONTRIBUTIONS

R.M. and V.S.S. designed the experiments and analyses. R.M. performed all experiments and analyzed the data, except that R.M. and Y.L. performed immunohistochemistry. S.S. generated pilot histology data for anterograde tracing experiments. R.M. and V.S.S. wrote the manuscript.

SUPPLEMENTAL INFORMATION

Supplemental information can be found online at https://doi.org/10.1016/j.cell.2022.04.001.

DECLARATION OF INTERESTS

The authors declare no competing interests.

Author Manuscript Author Manuscript Author Manuscript Author Manuscript

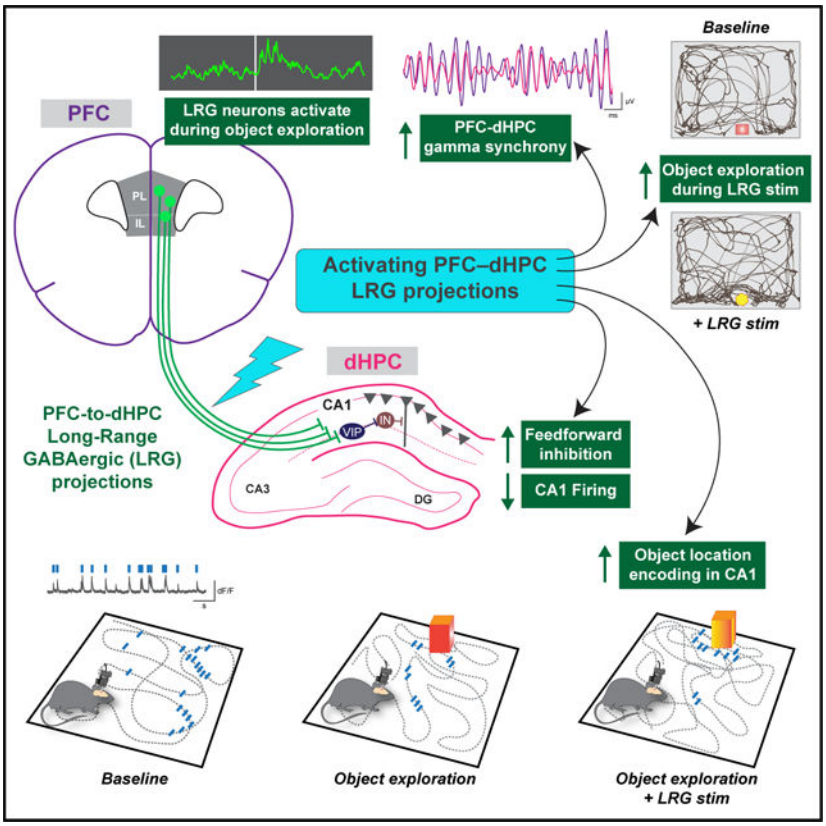

INTRODUCTION

The prefrontal cortex (PFC) is postulated to communicate bidi-rectionally with many cortical and subcortical brain regions, providing top-down control of behavior by monitoring and gating brain activity (Gazzaley and D'Esposito, 2007; Miller and Cohen, 2001; Miller, 2000). One such region is the hippocampus (HPC), a key node for processing spatial information to guide behavior. PFC-HPC network interactions play a key role in cognitive and emotional behaviors (Eichenbaum, 2017; Jin and Maren, 2015; Preston and Eichenbaum, 2013; Shin and Jadhav, 2016; Sigurdsson and Duvarci, 2016; Yu and Frank, 2015). Conversely, abnormal PFC-HPC interactions are implicated in several neuropsychiatric disorders, including schizophrenia, depression, and anxiety (Cunniff et al., 2020; Godsil et al., 2013; Kupferschmidt and Gordon, 2018; Li et al., 2015; Sigurdsson et al., 2010).

Studies in humans and rodents have shown that concurrent activity in, and communication between, the PFC and HPC is essential for exploratory behaviors (Bähner et al., 2015; Churchwell et al., 2010; DeVito and Eichenbaum, 2010; Floresco et al., 1997; Wang and Cai, 2006; Yoon et al., 2008). Neural activity and network oscillations synchronize across the PFC and HPC during exploration (Colgin, 2011; Jones and Wilson, 2005; O'Neill et al., 2013; Spellman et al., 2015). Oscillatory activity in HPC leads PFC when rats explore spatial contexts, but this switches to PFC leading when rats explore objects (Place et al., 2016) or arrive at decision points in a maze (Hallock et al., 2016). Furthermore, PFC

Author Manuscript Author Manuscript Author Manuscript Author Manuscript

inactivation alters spatial encoding in the HPC (Guise and Shapiro, 2017; Kyd and Bilkey, 2003). These findings suggest that the PFC exerts top-down control over HPC activity at key behavioral timepoints, but knowledge about direct anatomical projections mediating this top-down control has been lacking. The only example of direct excitatory-to-excitatory connectivity from PFC to HPC is a sparse projection from the anterior cingulate cortex (ACC) (Rajasethupathy et al., 2015). This stands in stark contrast to the much more extensive direct projections from HPC-to-PFC (Hoover and Vertes, 2007; Jay and Witter, 1991). As a result, most top-down communication in the PFC-to-HPC direction has been assumed to occur indirectly, via the thalamic nucleus reuniens (NR) (Vertes et al., 2007; Xu and Südhof, 2013). Not only are the anatomical substrates for top-down control unknown, the manner in which top-down control operates is also unclear, i.e., does the PFC transmit specific information, e.g., representations of specific actions or goals, or alternatively, does it modulate network dynamics and emergent computations in HPC?

Growing evidence indicates that cortical and hippocampal circuits include long-range projecting GABAergic (LRG) inhibitory neurons (Basu et al., 2016; Jinno et al., 2007; Melzer and Monyer, 2020; Tamamaki and Tomioka, 2010). In some cases, these LRG projections have been shown to control oscillatory synchrony between structures (Christenson Wick et al., 2019; Francavilla et al., 2018; Melzer et al., 2012), suggesting that they may be important regulators of interregional communication. We recently reported that the PFC contains LRG projection neurons capable of influencing behavior (Lee et al., 2014). Here, we describe how the PFC exerts top-down control over information processing in the HPC by acting through a unique circuit motif: long-range GABAergic projections that inhibit disinhibitory microcircuits, thereby altering emergent network dynamics and promoting specific exploratory behaviors.

RESULTS

Hippocampus-projecting long-range GABAergic (LRG) neurons in the PFC

To label potential PFC-to-HPC LRG projections, we injected AAV to drive Cre-dependent expression of eYFP in the PFC of *Dlxi12b-Cre* mice (Figure 1A) (Lee et al., 2014; Potter et al., 2009). After waiting for viral transduction, we observed robust eYFP expression in the cell bodies of PFC GABAergic neurons and also observed many axonal fibers in the CA1 and dentate gyrus subfields of dHPC (Figures 1B, S1A, and S1B). Importantly, no eYFP+ cell bodies were observed in the HPC. Next, we asked whether these PFC LRG axon terminals synapse onto dHPC neurons. For this, we expressed ChR2-eYFP in PFC GABAergic neurons and made *ex vivo* recordings from acute hippocampal slices (Figure 1C). Notably, optogenetic activation of PFC LRG axonal fibers in dHPC slices elicited robust short-latency postsynaptic currents (oPSCs) in dHPC neurons. These currents reversed at the GABA reversal potential, were not affected by glutamatergic receptor antagonists, and were completely blocked by the $GABA_A$ receptor antagonist gabazine (Figure 1D).

Following the identification of PFC–dHPC LRG projections, we asked whether dHPC-projecting PFC LRG neurons have distinct physiological and molecular properties. We used an intersectional strategy to selectively express ChR2-eYFP in dHPC-projecting PFC

Author Manuscript Author Manuscript Author Manuscript Author Manuscript

LRG neurons (Lee et al., 2014) (Figures 1E and 1F). We then made *ex vivo* patch clamp recordings from eYFP+ LRG neurons in prefrontal slices and recorded reliable short-latency light-evoked action potentials (APs) to confirm they expressed ChR2 (Figure 1G). The dHPC-projecting PFC LRG population was physiologically diverse, comprising neurons with regular spiking (9/16 neurons), irregular spiking (3/16 neurons), and fast spiking (4/16 neurons) properties (Figure 1H and Table S1). Furthermore, dHPC-projecting PFC LRG neurons were distributed across superficial and deeper layers of the prelimbic (PL) and infralimbic (IL) portions of the PFC. To characterize the molecular identity of these LRG neurons, we injected a retrograde tracer (Alexa 594-tagged CTb) in dHPC and performed immunohistochemistry in prefrontal sections (Figures S1C and S1D). dHPC-projecting PFC LRG neurons include parvalbumin (PV), somatostatin (SST), and vasoactive intestinal polypeptide (VIP)-expressing subpopulations, as well as small percentages of calretinin (CR) and neuropeptide-Y (NPY) expressing neurons (Figures S1E and S1F).

To confirm the molecular diversity of dHPC-projecting prefrontal LRG neurons, we utilized a modified intersectional strategy (see STAR Methods) to label dHPC projecting prefrontal GABAergic neurons in SST-Cre, PV-Cre, and VIP-Cre mice (Fig. S2A). Similar to our findings in *Dlxi12b-Cre* mice, the anatomical tracing analysis using the *SST-Cre*, *PV-Cre*, and *VIP-Cre* mouse lines also showed eYFP+ GABAergic cell bodies in the PFC and eYFP+ axon terminals in the dHPC (Figure S2B). Our analysis also revealed sparse axon collaterals of PFC–dHPC LRG neurons to other cortical and subcortical brain regions (Figure S2C and Table S2). Together, these results illustrate that a heterogeneous population of prefrontal GABAergic neurons sends direct projections to dHPC.

PFC LRG projections target hippocampal disinhibitory interneurons

Next, we asked how these PFC LRG projection neurons affect circuit computations in the CA1 subregion, the primary output region for HPC. Specifically, we asked whether PFC LRG projections target specific CA1 cell-types. We expressed ChR2-eYFP in PFC LRG projections and obtained *ex vivo* patch clamp recordings from excitatory pyramidal neurons (PNs) and GABAergic interneurons (INs) located in different topographical layers of CA1 subregion (Figure 2A). Interestingly, we observed robust optogenetically-evoked IPSCs in CA1 INs (55/70 connected, henceforth referred to as recipient INs), but not in CA1 PNs (0/38 connected). Many of the recipient CA1 INs were located near the border between stratum radiatum (SR) and stratum lacunosum-moleculare (SLM) (Figure 2B). Recipient CA1 INs were also physiologically heterogeneous including regular spiking, irregular spiking, and fast spiking subtypes (Figure 2B and Table S3). To determine the molecular identities of these recipient INs, we filled a subset of them with biocytin and quantified immunoreactivity for three molecular markers commonly expressed in CA1 INs: PV, SST, and VIP. Surprisingly, most recipient INs expressed VIP (7/11). By contrast, none expressed PV or SST (0/10) (Figure 2C).

PFC LRG projections regulate excitatory input integration in CA1 microcircuit

Since VIP is predominantly expressed by interneuron-selective interneurons (ISIs) which produce circuit disinhibition in CA1 (Acsády et al., 1996a, 1996b; Chamberland and Topolnik, 2012; Turi et al., 2019), we hypothesized that PFC–dHPC LRG projections may

Author Manuscript Author Manuscript Author Manuscript Author Manuscript

inhibit VIP+ ISIs, thereby reducing disinhibition and increasing feedforward inhibition in the CA1 microcircuit. To test this, we quantified the effect of optogenetic stimulation of PFC LRG projections on excitatory and inhibitory postsynaptic potentials (EPSPs and IPSPs) elicited by two major afferent input pathways: Schaffer collateral (SC) and temporoammonic (TA) inputs (Figure 2D). Specifically, during patch clamp recordings from CA1 PNs, we electrically stimulated SC or TA inputs concomitant with optogenetic stimulation of ChR2+ PFC–dHPC LRG axon fibers. While optogenetic stimulation of PFC–dHPC LRG axons alone did not elicit discernable postsynaptic potentials in CA1 PNs, concomitant electrical and optogenetic stimulation significantly increased the size of IPSPs relative to EPSPs for both SC and TA inputs (Figures 2E, 2F, and S3A–S3C). This reduction in the excitation to inhibition ratio (E/I ratio) for SC and TA inputs is consistent with our prediction and suggests that the PFC LRG projections increase feedforward inhibition by inhibiting disinhibitory VIP+ ISIs in CA1. It is important to note that while the E/I ratio for both SC and TA inputs was lowered by activation of prefrontal LRG projections, the relative change in EPSPs and IPSPs differed for the two pathways. Reduction in SC pathway E/I ratio was driven by significantly reduced EPSPs, whereas the reduction in TA pathway E/I ratio was largely mediated by increased IPSPs. This suggests that prefrontal LRG projections might differentially target CA1 INs associated with SC and TA inputs (Freund and Buzsaki, 1996; Pelkey et al., 2017).

Next, we asked whether the increased feedforward inhibition and reduced E/I ratio elicited by PFC LRG projections affects the input-output transformation of CA1 PNs. Coincident activation of SC and TA input pathways, often in a theta-burst stimulation (TBS) pattern, causes supralinear summation and spiking in CA1 PNs (Ang et al., 2005; Bittner et al., 2015; Malik and Johnston, 2017). This nonlinear integration and coincidence detection by CA1 PNs is tightly regulated by the activity of CA1 INs and considered crucial for hippocampal information processing (Grienberger et al., 2017; Milstein et al., 2015). To determine how PFC–dHPC LRG projections modulate input integration in CA1 PNs, we combined electrical TBS of SC and TA inputs with optogenetic stimulation of PFC–dHPC LRG projections (Figure 2G). Again, consistent with increased feedforward inhibition, optogenetic stimulation of LRG projections reduced firing and EPSP summation during TBS (Figure 2H). Importantly, CA1 PN firing in response to depolarizing current injections (i.e., depolarization without recruitment of microcircuit inhibition) was not affected by optogenetic stimulation of PFC LRG projections (Figure S3D). Taken together, our *ex vivo* electrophysiological analyses show how PFC–dHPC LRG projections regulate synaptic integration and input-output gain by enhancing feedforward inhibition onto CA1 PNs (Figure S3E).

PFC–dHPC LRG projection neurons activate during object exploration behavior

PFC-HPC communication is implicated in exploratory behaviors (DeVito and Eichenbaum, 2010; Jin and Maren, 2015; Preston and Eichenbaum, 2013; Spellman et al., 2015; Yu and Frank, 2015). Both structures synchronize at theta frequency with dHPC leading when rodents enter a spatial context, but the directionality switches to PFC leading when animals sample an object (Place et al., 2016). This suggests an important role for PFC-to-dHPC top-down communication during object exploration, potentially mediated by prefrontal LRG

Author Manuscript Author Manuscript Author Manuscript Author Manuscript

neurons. To study this, we selectively expressed GCaMP6m in the PFC–dHPC LRG neurons (Figures 3A–3D) and performed bulk Ca^{2+} fiber photometry while mice explored a novel object in their environment. Analysis of GCaMP6m activity time-locked to the start of object interaction bouts showed increased activity of the PFC–dHPC LRG neurons when mice approach and explore novel objects (Figures 3E–3G). Interestingly, we observed similar object exploration-related activity when we non-specifically labeled all prefrontal inhibitory neurons (see STAR Methods) (Figures 3B and 3H–3J). In line with the known role of PFC GABAergic neurons in social behavior (Scheggia et al., 2020; Yizhar et al., 2011), activity of PFC–dHPC LRG projection neurons, as well as that of non-specifically labeled PFC inhibitory neurons, also increased during exploration of stationary social targets (Figure S4A). These results suggest that the activity of PFC GABAergic neurons is tightly linked to exploratory behaviors, and PFC–dHPC LRG projections provide a pathway for transmitting this time-locked prefrontal activity to dHPC.

PFC–dHPC LRG projections regulate object exploration Next, we asked whether *in vivo* optogenetic manipulation of PFC–dHPC LRG projections affects exploratory behaviors. We first quantified the effects of optogenetic stimulation by virally expressing ChR2 in PFC–dHPC LRG projections (Figure 4A). Optogenetic stimulation of PFC–dHPC LRG projections (20 Hz) dramatically increased the time ChR2 expressing-mice spent exploring a novel object (Figures 4B and 4C). Increases in NOE occurred both early and late during the testing session and reflected increases in both short- and long-duration exploratory bouts (Figure 4D).

Previous studies have suggested that interactions between PFC and HPC are important for discriminating novel vs. familiar objects (Barker et al., 2007; DeVito and Eichenbaum, 2010; Eichenbaum, 2017; Warburton and Brown, 2015). We tested how stimulating these projections during sample and test phases of the object-recognition task affects recognition memory (Figures S4B–S4E). Stimulating PFC–dHPC LRG projections increased exploration of both objects, without affecting the preference for novel vs. familiar objects. We also asked whether dHPC-projecting PFC LRG projection neurons might influence the exploration and/or preference related to spatial and social targets. Optogenetic stimulation of PFC–dHPC LRG projections had no effect on open field exploration (Figure S4F), real-time place preference (RTPP) (Figure S4G), or time spent in social interaction (Figures S4H–S4J). Together these experiments suggest that activating PFC–dHPC LRG projections specifically increases object exploration behavior.

To establish a causal role of PFC–dHPC LRG projections in NOE behavior, we optogenetically inhibited these projections while mice explored a novel object (Figure 4E). Since PFC–dHPC LRG projection neurons specifically increase activity during object exploration bouts, we optogenetically silenced these projections (using inhibitory opsin eNpHR3.0) when mice entered the “object zone” – a small rectangular zone surrounding the object (Figure 4F). Closed-loop optogenetic silencing of these projections reduced both the exploration time and the number of exploration bouts during NOE (Figures 4G–H), i.e., the opposite of what we observed during optogenetic stimulation. Somewhat surprisingly, continuous inhibition of LRG projections during a 5 min testing period had no effect on NOE (Figures S5A and S5B). This discrepancy between the effects of closed-loop vs.

Author Manuscript Author Manuscript Author Manuscript Author Manuscript

continuous inhibition of LRG projections could reflect physiological or technical factors. Inhibition might be most effective when it specifically blocks the normal recruitment of these projections during object approaches. Continuous stimulation might also lead to eNpHR inactivation (Mattis et al., 2012; Wiegert et al., 2017), which could blunt behavioral effects during continuous stimulation.

In a control experiment, closed-loop inhibition of PFC–dHPC LRG projections had no effect on exploration or preference for a randomly assigned "stimulation zone" (with no objects) (Figures S5C–S5F). These findings further establish that PFC–dHPC LRG projections have a specific role in object exploration, but not in all exploratory behaviors.

PFC–dHPC LRG projections promote network oscillations associated with object exploration

What are the potential circuit mechanisms through which PFC–dHPC LRG projections might impact NOE? To address this, we recorded local field potentials (LFPs) to determine whether stimulation of PFC–dHPC LRG projections might induce network states conducive to NOE. In comparison to baseline home cage (HC) exploration, NOE recruited synchronized oscillations in the low-gamma (25–55 Hz) band across the PFC-dHPC network. Specifically, during NOE we observed a significant increase in low-gamma power in both structures as well as an increase in PFC-dHPC low-gamma phase synchrony (Figures 5A–5D). While increased low-gamma activity was most prominent, NOE was also associated with significant increases in power (but not synchrony) for high-gamma and theta activity (Figure 5D and Table S4). The NOE related change in low-gamma oscillations is particularly notable because previous studies have shown that object exploration increases low-gamma synchrony between hippocampal subfields (Trimper et al., 2017).

Since interactions between CA1 INs and PNs critically regulate gamma oscillations (Csicsvari et al., 2003; Tukker et al., 2007), we hypothesized that by modulating microcircuit inhibition, PFC–dHPC LRG projections could contribute to NOE-associated changes in gamma activity. To test this, we next combined optogenetic stimulation with LFP recordings in mice expressing ChR2 in PFC–dHPC LRG projections (Figure 5E). Indeed, optogenetic stimulation of PFC LRG terminals in dHPC mimicked the increase in low-gamma phase synchrony observed during NOE (Figure 5H). Significant shifts in LFP power were also observed during optogenetic stimulation of PFC LRG terminals (Figures 5F–5H and Table S4). This suggests a preferential role of these projections in PFC-dHPC gamma synchrony.

Finally, to test whether object exploration-induced low-gamma synchrony is blocked by inhibiting PFC–dHPC LRG projections, we analyzed LFPs recorded in the dHPC and PFC during closed-loop optogenetic inhibition of the PFC LRG projections (Figures 5I and 5J). Consistent with our finding that object exploration is associated with increased low-gamma phase synchrony, PFC-dHPC low-gamma phase synchrony increased when control mice explored an object in the Laser ON zone. By contrast, in eNpHR-expressing (*Dlxi12b-Cre+*) mice, inhibiting PFC–dHPC LRG projections eliminated object exploration-induced low gamma synchrony (Figure 5K). We also examined object exploration-induced increases in gamma power within the PFC and dHPC (Table S4). In control mice, we again observed

Author Manuscript Author Manuscript Author Manuscript Author Manuscript

significant increases in dHPC and PFC power during bouts of object exploration. However, the magnitude of this increase in PFC gamma power was significantly attenuated by closed-loop optogenetic inhibition in *Dlxi12b-Cre+* mice (based on a two-way ANOVA comparing PFC gamma power during object exploration vs. outside the object zone in control vs. *Dlxi12b-Cre+* mice, $p = 0.04$). Furthermore, we observed a non-significant decrease in dHPC gamma power during closed-loop optogenetic inhibition in *Dlxi12b-Cre+* mice. These results suggest that PFC–dHPC LRG projections may contribute to object exploration by promoting PFC-dHPC low-gamma synchrony.

PFC–dHPC LRG projections reduce hippocampal activity *in vivo*

We next asked how LRG projections affect NOE-associated neuronal activity in dHPC. For this, we used miniaturized microscopes to record Ca^{2+} activity in CA1 neurons while mice explored novel objects. Concurrently, we expressed the red-shifted excitatory opsin ChrimsonR in PFC–dHPC LRG projections (Klapoetke et al., 2014; Stamatakis et al., 2018) (Figures 6A–6D). On day 1, mice explored a novel object in the absence of any optogenetic stimulation. Overall Ca^{2+} activity decreased significantly during NOE, relative to the HC epoch (Figure 6E), although 25/97 neurons had higher activity during NOE. On day 2, we optogenetically stimulated PFC–dHPC LRG projections during both HC and NOE epochs. Compared to the pre-stimulation HC period, stimulating LRG projections significantly reduced activity of CA1 neurons. Activity was then further reduced during subsequent NOE (Figure 6E). Notably, light delivery alone did not influence the overall activity of CA1 neurons in opsin-negative control mice (Figure 6F; % neurons with reduced activity during HC + LRG stimulation epoch: 72% in *Dlxi12b-Cre+* mice vs. 51% in Cre-negative mice; Chi-square test, $p < 0.05$). Overall, this reduction in population activity is consistent with our *ex vivo* observation that activating PFC–dHPC LRG projections enhances feedforward inhibition and reduces spiking in CA1 PNs.

We performed longitudinal analysis of neurons recorded on both imaging days (referred to as registered neurons). Specifically, we compared the activity of registered neurons across days during the HC and NOE epochs (Figures S6B and S6C). We found that the day 1 and day 2 activities in HC epoch were highly correlated for registered neurons in all mice (Figures S6D and S6E). However, NOE epoch activity on day 1 and day 2 was highly correlated for registered neurons in control mice, but not *Dlxi12b-Cre+* (ChrimsonR-expressing) mice (Figures S6F and S6G). In line with the overall reduction in population-level activity we previously noted with LRG stimulation, stimulating PFC–dHPC LRG projections on day 2 reduced the activity of registered neurons during NOE in *Cre+* mice.

PFC–dHPC LRG projections enhance hippocampal object encoding

To assess whether these population-level changes in CA1 activity were associated with altered encoding of NOE-relevant information, we compared NOE-driven changes in neuronal activity on day 1 (no stimulation) vs. day 2 (LRG stimulation). As shown by the seminal discovery of place cells, dHPC CA1 neurons encode information by preferentially firing in specific spatial locations (Moser et al., 2008; O'Keefe, 1976; Wilson and McNaughton, 1993). Importantly, previous work suggests that hippocampal CA1 neurons

Author Manuscript Author Manuscript Author Manuscript Author Manuscript

represent non-spatial features and objects by changing their encoding properties near these landmarks (Knierim, 2002; O'Keefe and Krupic, 2021). We asked whether PFC–dHPC LRG projections affect the encoding properties of hippocampal neurons near the object location. Specifically, for each neuron, we defined its "object signal-to-noise ratio" (Object_SNR) as the change in its activity within a zone surrounding the object location (z-scored to the mean and standard deviation outside the object zone) before vs. after introducing the object (Figure 7A). Based on this metric, neurons that increased or decreased activity in the object zone by one standard deviation had Object_SNR of 1 or −1, respectively. During light stimulation, the activity of neurons decreased both within and outside of the object zone; the standard deviations of neuronal activity also decreased (Figure 7B). Depending on exactly how these changes were distributed across neurons, Object_SNR values could potentially increase, decrease, or remain unchanged. In fact, stimulating PFC LRG projections significantly increased Object_SNR values relative to the no light condition (Figures 7C and S6I). Notably, light delivery alone did not affect the Object_SNR in control mice (Figures 7C and S6H, and Table S5). Furthermore, LRG stimulation did not affect an analogous "SNR" calculated for control zones on the opposite side of the cage (instead of the object zone) (Figures 7D–7F and Table S5). Thus, even though PFC–dHPC LRG projections potentiate feedforward inhibition and reduce overall network activity, their net effect on hippocampal encoding is to specifically enhance SNR of CA1 neuronal activity at object locations.

While the above analysis illustrates how PFC–dHPC LRG projections influence the encoding of hippocampal CA1 neurons at object locations, it does not account for whether neurons have significant spatial tuning, i.e., are place cells. To address this, we classified the imaged neurons on days 1 and 2 as place cells vs. non-spatial cells (STAR Methods). We then analyzed the effects of NOE and PFC–dHPC LRG projection stimulation on place field (PF) properties. Studies on place cells often provide water/food rewards to encourage exploration of the entire environment (Kinsky et al., 2018; Meshulam et al., 2017; Stefanini et al., 2020; Ziv et al., 2013). Our study exploited the natural tendency of mice to explore novel stimuli in their environment but did not include such rewards. Even with this potential caveat that some portions of the test cage may have been underexplored, we found well-defined PFs for many CA1 neurons (Figures S7A and S7B). Introducing an object increased the spatial information and reduced the sparsity index of CA1 place cells (consistent with Bourboulou et al., 2019; Burke et al., 2011) (Tables S6 and S7). Strikingly, stimulating LRG projections dramatically enhanced object-induced increases in spatial information of place cells–an effect not observed in control (opsin-negative) mice. Furthermore, during stimulation of PFC LRG projections, the remapping distance (shifts in PF centroid caused by introducing the object) was inversely correlated with the PF centroid distance from the object location during NOE (Figure 7G). Similar correlations were not observed without optogenetic stimulation (Figure 7H). Together, these analyses highlight how PFC–dHPC LRG projections regulate hippocampal spatial encoding (Figure 7I).

DISCUSSION

Here, we describe a monosynaptic projection from the PFC-to-dHPC. There are many unusual features of this projection: it is GABAergic and targets hippocampal VIP+ ISIs,

Author Manuscript Author Manuscript Author Manuscript Author Manuscript

thus representing a “doubly disinhibitory” long-range motif. This projection modulates microcircuit dynamics in the CA1 region of dHPC, increasing feedforward inhibition, reducing spiking evoked by afferent inputs while enhancing low-gamma synchrony between the PFC and dHPC. In accord with the postulated role of PFC as a top-down controller, activating these projections specifically enhances object-related spatial encoding in the dorsal CA1 and drives object exploration. Overall, our study shows that these top-down prefrontal projections can dynamically control the network state and emergent circuit function in the dHPC, thereby altering the signal-to-noise ratio for specific neural representations and eliciting corresponding changes in behavior.

Relationship to previous work

Many studies have suggested that PFC exerts top-down control over information processing in the HPC, particularly during behaviors involving spatial and object exploration (Brincat and Miller, 2015; Eichenbaum, 2017; Jin and Maren, 2015; Place et al., 2016; Preston and Eichenbaum, 2013; Shin and Jadhav, 2016; Sigurdsson and Duvarci, 2016; Yu and Frank, 2015). Lesion and pharmacological inactivation of PFC severely impairs spatial navigation and object exploratory behaviors, and also disrupts neuronal encoding in the HPC (Churchwell et al., 2010; DeVito and Eichenbaum, 2010; Floresco et al., 1997; Guise and Shapiro, 2017; Kyd and Bilkey, 2003; Wang and Cai, 2006; Yoon et al., 2008). Nevertheless, pathways mediating prefrontal top-down control have not been identified, and it was not known whether the PFC acts by transmitting specific information to the HPC vs. modulating the network state and emergent circuit function. Our study addresses this major gap. Based on their anatomical targeting and microcircuit effects, the PFC–dHPC LRG projections we describe are also well positioned to potentially mediate PFC-to-hippocampus communication during inhibitory control of actions and processes involved in memory retrieval (Anderson et al., 2016). These direct GABAergic PFC-dHPC projections may transmit information in parallel to indirect projections from the PFC to ventral HPC mediated by the NR (Hoover and Vertes, 2012; Varela et al., 2014), and direct glutamatergic projections from the ACC to dHPC (Rajasethupathy et al., 2015). Similar to other LRG inputs to HPC, PFC–dHPC LRG projections target inhibitory interneurons. However, whereas PFC–dHPC LRG projections increase feedforward inhibition by inhibiting VIP interneurons, LRG projections from entorhinal cortex target local HPC INs and reduce feedforward inhibition (Basu et al., 2016; Melzer et al., 2012).

Conclusions

Our study describes an anatomical pathway that plays a key role in direct PFC-to-HPC communication. The unique features of these projections (i.e., long-range GABAergic, disinhibitory IN targeting) enable PFC to dynamically alter emergent network activity and information processing in the HPC and thereby exert top-down control over exploratory behavior.

Limitations of the study

Since PFC–dHPC LRG neurons comprise molecularly diverse subtypes (e.g., PV, SST, and VIP expressing), future studies could use subtype-specific Cre-driver lines to determine

Author Manuscript Author Manuscript Author Manuscript Author Manuscript

whether these subtypes perform similar vs. distinct circuit functions. While we found that PFC–dHPC LRG projections primarily target VIP-expressing hippocampal interneurons, increase feedforward inhibition, and reduce overall hippocampal activity, we do not yet completely understand how this ends up enhancing low-gamma synchrony and object-related spatial encoding. In particular, CA1 VIP+ ISIs are diverse (Acsády et al., 1996a, 1996b; Chamberland and Topolnik, 2012). Thus, it may be necessary to identify the sources of input to, and post-synaptic targets of, the CA1 VIP ISIs which receive direct PFC LRG input.

These targets of LRG-recipient neurons in CA1 may be driven by specific inputs (TA vs. SC) and/or target specific pyramidal neuron dendritic compartments. VIP ISIs that receive PFC LRG input might also send long-range projections to different parts of the hippocampal formation, and/or participate in specific oscillations (Francavilla et al., 2018), contributing to the changes in network dynamics we observed.

STAR★METHODS

RESOURCE AVAILABILITY

Lead contact—Further information and requests for resources and reagents should be directed to and will be fulfilled by the lead contact, Vikaas S. Sohal (vikaas.sohal@ucsf.edu).

Materials availability—This study did not generate any new reagents.

Data and code availability

- All data reported in this paper will be shared by the lead contact upon request.
- Custom data analysis code has been deposited in a Github repository and is publicly available as of the date of publication. The URL is listed in the Key Resources table.
- Any additional information required to reanalyze the data reported in this paper is available from the lead contact upon request.

EXPERIMENTAL MODEL AND SUBJECT DETAILS

Mice—All animal care procedures and experiments were conducted in accordance with the National Institutes of Health guidelines and approved by the Administrative Panels on Laboratory Animal Care at the University of California, San Francisco. Mice were housed in a temperature-controlled environment (22–24°C) with *ad libitum* access to food and water. Mice were reared in normal lighting conditions (12-h light/dark cycle). Male and female mice (5–6 weeks old at the time of initial surgeries) from the following lines were used: *Dlxi12b-Cre* (Potter et al., 2009), *PV-Cre* (The Jackson Lab), *SST-IRES-Cre* (The Jackson Lab), *VIP-Cre* (The Jackson Lab), and wild-type CD-1.

Author Manuscript Author Manuscript Author Manuscript Author Manuscript

METHODS DETAILS

Virus and retrograde tracer injections—Mice were anesthetized with isoflurane and placed on a stereotaxic frame (David Kopf Instruments). An incision was made to expose the skull, and bregma and lambda were used as references to align the skull. Body temperature was maintained using a heating pad. Virus was injected (at the rate of 100 nL/min) with a microinjection syringe (Nanofil 10 μL with 35 gauge needle, World Precision Instruments) connected to a microsyringe pump (World Precision Instruments, UMP3 UltraMicroPump). Coordinates for injections into PFC were (in mm, relative to Bregma) 1.8 anterior-posterior (AP), ±0.3 mediolateral (ML), −2.4 dorsoventral (DV); and coordinates for injections into dHPC were −1.35 AP, ±0.65 ML, −1.5 DV.

For anterograde tracing, *ex vivo* slice physiology, and optogenetic stimulation experiments, either AAV5-EF1α-DIO-eYFP virus or AAV5-EF1α-DIO-ChR2-eYFP virus (UNC Vector core, 650 nL) was injected into PFC of *Dlxi12b-Cre+* mice and Cre-negative mice. For optogenetic inhibition experiments, AAV5-EF1α-DIO-eNpHR3.0-mcherry virus (UNC Vector core, 650 nL) was injected into the PFC. For intersectional labeling of dHPC-projecting PFC LRG neurons, CAV2-Cre virus (del Rio et al., 2019; Hnasko et al., 2006) (650 nL) was injected in the dHPC and AAV5-Dlxi12b-BG-DIO-ChR2-eYFP virus (Lee et al., 2014) (650 nL) was injected in the PFC of CD-1 mice. For retrograde labeling of dHPC-projecting PFC LRG neurons, Alexa Flour 594 Cholera toxin beta subunit conjugate (CTb-594, Invitrogen; 0.5% w/v, 400–500 nL) was injected in dHPC of CD-1 mice. After virus or tracer injection, the microinjector needle was left in place for 5–6 min before being removed from the brain. Mice were sutured (if receiving viral/tracer injection only) and were allowed to recover on a heated pad until ambulatory.

Optic fiber implantation—Following bilateral AAV5-EF1α-DIO-ChR2-eYFP or AAV5-EF1α-DIO-eNpHR3.0-mcherry virus injections in PFC, dual fiber-optic cannulas (Doric lenses; 200/240 mm, 0.22NA) were implanted in dHPC (−1.35 AP, ±0.65 ML, −1.4 DV). During these surgeries, the skull was scored with a scalpel to improve implant adhesion. We waited at least 7 weeks after surgery to allow time for viral expression.

Fiber photometry: Data acquisition and analysis—For expressing GCaMP in dHPC-projecting PFC GABAergic neurons, *Dlxi12b-Cre+* mice received unilateral injections of AAV8-CON/FON-GCaMP6m virus (Addgene) (Fenno et al., 2014) in the PFC and AAVretro-EF1a-Flpo (Addgene) in the dHPC. After virus injections, mono fiber-optic cannulas were implanted in the PFC. Likewise, for measuring activity of non-specifically labeled PFC GABAergic neurons, *Dlxi12b-Cre+* mice received unilateral injections of 1:3 diluted AAV8-Syn-flex-GCaMP6m (Addgene) in the PFC followed by implantation of mono fiber-optic cannulas. Fiber photometry experiments were conducted 7–8 weeks after surgery.

The photometry recording apparatus design was similar to previous studies (Cho et al., 2020). Blue excitation light at 470 nm was used to stimulate GCaMP6m fluorescence and isosbestic signal recorded in response to a violet excitation light (405 nm) was used to correct for bleaching and perform ratiometric measurements of GCaMP6m

Author Manuscript Author Manuscript Author Manuscript Author Manuscript

activity. Accordingly, two excitation LEDs (470 nm and 405 nm, Thorlabs M470F1 and M405FP1) were connected to a mini cube (Doric Lenses, FMC2_Af405-GCaMP_FC) by a patch cord (200 μm core, NA = 0.39, Doric Lenses) and controlled by an LED driver (Thorlabs DC4104), and connected to an RX-8 real-time processor (Tucker Davis Technologies). The GCaMP6m signal was collected through a low auto-fluorescence patch cord (Doric Lenses, MFP_600/630/LWMJ-0.48_0.5m_FC-FC) and focused onto a photoreceiver (Newport, Model 2151). The modulated signals generated by the two LEDs were independently recovered using standard synchronous demodulation techniques implemented on the RX-8 real-time processor. A computer installed with Synapse software (Tucker-Davis Technologies) was used to control the photometry data acquisition, and to record synchronized behavior video. Data analysis was performed using custom scripts written in MATLAB.

Using a least-squares linear fit, the 470 nm signal was aligned to the 405 nm control signal. The *dF/F* time series was then calculated as: ((470 nm signal - fitted 405 nm signal) / fitted 405 nm signal). dF/F values were converted to z-scored dF/F using the average and standard deviation of the signals during the behavior testing session. For measuring changes in GCaMP6m signals during NOE behavior, mouse behavior was manually scored, and NOE bout start times were marked. Peak z-scored dF/F values 5 s before and after NOE bout start were compared. Data points in plots shown in Fig. 3G and J were calculated by averaging the z-scored dF/F values from all NOE bouts for every mouse.

Optogenetic stimulation of PFC–dHPC LRG projections—A 473 nm blue laser (OEM Laser Systems, Inc.) was coupled to the dual fiber-optic cannula (implanted in dHPC) through a dual fiber-optic patch cord (Doric Lenses, Inc.), and was controlled via a function generator (Agilent 33500B Series Wave-form Generator). Laser power was adjusted such that the final light power was 3–4 mW total, summed across both fibers, and averaged over 20 Hz light pulses (5 ms duration).

Closed loop optogenetic inhibition of PFC–dHPC LRG projections during novel object exploration—Mice were habituated to a large housing cage (48 × 35 cm) for 2–3 days. On testing day, mice were placed in the cage and were allowed to freely explore for 10 min. After this baseline period, a novel object was added to the cage and mice were allowed to explore the object for 12 min. During the NOE testing, area surrounding the object (24 × 12 cm) was assigned as the ‘Laser ON Zone’ and the remaining area was called the ‘Laser OFF Zone’. Mouse positions were tracked using ANY-maze software connected to a green laser (532 nm). Laser was coupled to the dual fiber-optic cannula (implanted in dHPC) through a dual fiber-optic patch cord (Doric Lenses, Inc.) (light power ~3 mW/fiber). Laser output was triggered by TTL pulses when mouse entered the Laser ON Zone and laser was turned off when mouse entered the Laser OFF Zone.

Behavioral assays—After sufficient time for surgical recovery and viral expression, mice were handled and habituated for multiple days (3–5 days). Briefly, mice were first habituated to the behavioral testing room for 30 min prior to handling each day. For 2–3 days before starting testing, mice were habituated to the cable tethers in their home cage for 15 min. The experimenter was blinded to experimental groups during behavioral testing and

Author Manuscript Author Manuscript Author Manuscript Author Manuscript

scoring. A USB webcam (Logitech) connected to a computer running ANY-maze (Stoelting Co.) was used to record behavior movies. The position of mice was tracked using the built-in tracking in ANY-maze software. In some experiments, mouse positions were tracked using trained neural networks in DeepLabCut open-source software package (Mathis et al., 2018).

Novel object exploration—For measuring novel object exploration, one previously unexplored object was placed in the home cage of an experimental mouse for 5 min. A blinded observer manually scored the following parameters: exploration time, bouts of exploration, and latency to the first exploration. Objects used in our study were usually lego toys, dice, small plumbing connectors, and falcon tube caps. For experimental mice with dual-fiber optic implants, two object interaction tests were performed over two days: day 1 testing was performed without light stimulation, and day 2 testing was done during optogenetic stimulation or inhibition of PFC–dHPC LRG projections. Cre-negative mice (no opsin control) with dual-fiber optic implants underwent similar behavior testing procedures.

Object recognition memory test: The task for object recognition memory was divided into habituation phase, sample phase, and test phase. During the habituation phase, mice were handled and habituated to the testing arena. In the sample phase, mice were allowed to explore two identical objects for 5 min. After a retention interval of 2 h, mice were returned to the arena for the test phase of the task. In this phase, one the previously explored objects was replaced with a novel object. Mice were allowed to sample the novel and familiar objects in the test phase for 5 min. The interaction time of the mice with objects in sample and test phases was manually scored and the ratio of the time spent exploring the novel and familiar object in the test phase was calculated.

The object recognition memory was tested twice in different open-field arenas (context 1 and context 2). In context 1 testing, mice receive optogenetic stimulation of PFC–dHPC LRG projection terminals during the sample phase of the task. In context 2 testing, optogenetic stimulation was delivered during the test phase.

Home cage social interaction test: For social interaction test, a novel juvenile (3–4 weeks old) mouse of the same sex was introduced in the home cage of an experimental mouse for 5 min. A blinded observer manually scored the time (in seconds) the experimental mouse spent with its nose in direct contact with the novel juvenile intruder. For all experimental mice, two social interaction tests were performed over two days: day 1 testing was performed without light stimulation, and day 2 testing was done during optogenetic stimulation of PFC LRG projections.

Three-chamber social interaction test: A Plexiglas box (57 × 24 × 23 cm) divided into three equal sized compartments was used as the testing apparatus. Inverted wire cups were placed in the end compartments for placing juvenile mice (social targets) during testing. The apparatus and wire cups were cleaned with 70% ethanol between sessions and after each test mouse.

The three-chamber social interaction test was divided into three phases: habituation, sociability, and social novelty. During the habituation phase, test mice were allowed to

Author Manuscript Author Manuscript Author Manuscript Author Manuscript

explore the apparatus for 10 min. During the sociability phase, a novel juvenile mouse was placed under one of the wire cups and the preference of the test mouse for the chamber with the juvenile mouse (social target) versus the empty wire cup was measured (10 min test duration). In the social novelty phase, the preference for a novel juvenile versus a familiar mouse was tested for 10 min. The PFC–dHPC LRG projections were optogenetically stimulated in the sociability and socialnovelty phases of the task.

Open field exploration test: Mice were placed in the center of a 50 × 50 cm open-field arena and were allowed to freely explore for 12 min. The testing time was divided into four (3 min) epochs. PFC–dHPC LRG projections were optogenetically stimulated during the 2nd and 4th epochs. Distance traveled during no stimulation (light OFF) and during optogenetic stimulation (light ON) epochs was quantified using the ANY-maze tracking software.

Real-time place preference (RTPP) test: Real-time place preference (RTPP) testing protocol consisted of three 20 min sessions conducted over 3 days. An apparatus with two identical chambers was used for RTPP testing. On day 1, mice were habituated to the apparatus for 20 min. On day 2, mice were placed into one randomly chosen chamber and the time spent in the two chambers was recorded. On day 3, one of the chambers was randomly assigned as the stimulated chamber. When mice entered this chamber, they received laser stimulation (optogenetic stimulation or inhibition of PFC–dHPC LRG projection terminals). The ratio of the time spent in the stimulated chamber vs. the non-stimulated chamber was used as the preference index. The sides used as the stimulated and non-stimulated chambers were counterbalanced across mice.

LFP recordings: Surgery and analysis

Surgery: Mice were anesthetized with isoflurane and placed on a stereotactic frame. After cleaning, the skull was scored with a scalpel to improve implant adhesion. For LFP recordings from wild-type CD-1 mice, tungsten electrodes (Microprobes) were inserted into the PFC (1.8 AP, −0.3 ML, −2.4 DV) and dHPC (−1.35 AP, −0.65 ML, −1.5 DV). For multisite LFP recordings combined with optogenetics, one LFP electrode was implanted after AAV5-EF1α-DIO-ChR2-eYFP or AAV5-EF1α-DIO-eNpHR3.0-mcherry virus injection into PFC of *Dlxi12b-Cre+* mice. A custom-made optrode (optical fiber + electrode) was implanted in dHPC to stimulate or inhibit PFC–dHPC LRG axon terminals during LFP recordings. To fabricate optrodes, a tungsten LFP recording electrode was affixed to one of the fibers of the dual-fiber optic cannula such that the tip of the electrode protruded 200–300 mm beyond the end the optic fiber (Lee et al., 2019). Reference and ground screws were implanted above the cerebellum. Electrodes and screws were cemented to the skull with Metabond (Parkell) and connected to a headstage for multi-channel recordings (Pinnacle). Following surgery, mice were monitored postoperatively, given analgesics, and individually housed.

Recording and analysis: LFP data were acquired at 2 KHz and band-pass filtered from 0.5–150Hz. Electrode placements were histologically confirmed. Analysis of LFP data was done using custom MATLAB (Mathworks) scripts. Briefly, signals were imported into MATLAB and LFP log power (for both channels) was calculated using the power spectral density

Author Manuscript Author Manuscript Author Manuscript Author Manuscript

output from the spectrogram function. For phase-synchrony analysis, LFPs were FIR-filtered for different frequency bands, then Hilbert transformed to yield the instantaneous amplitudes and phases. The following frequency bands were compared: theta band (4–12 Hz), beta band (15–25 Hz), low-gamma band (25–55 Hz), and high-gamma band (65–85 Hz).

To detect nonzero phase interdependencies (phase synchrony) between LFP signals recorded at PFC and dHPC electrodes, we estimated the weighted Phase Lag Index (wPLI) (Vinck et al., 2011) using the imaginary component of the cross-spectrum (S_{xy}) (Equations 1.1 and 1.2). A_x and A_y are instantaneous amplitudes; and ϕ_x and ϕ_y are instantaneous phases for PFC and dHPC signals, respectively.

$$S_{xy} = A_x A_y e^{i(\varphi_x - \varphi_y)} \quad \text{(Equation 1.1)}$$

$$wPLI = \frac{\sum |imag(S_{xy})| \operatorname{sgn}(S_{xy})|}{\sum |imag(S_{xy})|} \quad \text{(Equation 1.2)}$$

Log power and wPLI were calculated over short time intervals (at least 3 s in duration), i.e., the intervals during which a mouse was actively exploring an object or matched intervals during baseline periods when the mouse was in its home cage.

To analyze the LFPs recorded during closed-loop optogenetic inhibition of PFC LRG projections, we first extracted the time intervals when the mouse was exploring an object in the object zone (zone where green laser for optogenetic inhibition was ON). Next, we extracted time intervals when the mouse was outside the object zone. These outside zone time intervals were further filtered to remove time points when the mouse was running toward / away from the object zone, in order to minimize potential confounds related to the speed of movement. Power and wPLI of PFC and dHPC LFPs during object zone and outside zone time intervals were calculated and compared.

Ex-vivo slice physiology

Slice preparation: Adult mice were anesthetized with an intraperitoneal injection of euthasol and transcardially perfused with an ice-cold cutting solution containing (in mM) 210 sucrose, 2.5 KCl, 1.25 NaH_2PO_4, 25 $NaHCO_3$, 0.5 $CaCl_2$, 7 $MgCl_2$, 7 dextrose (bubbled with 95% O_2–5% CO_2, pH ~7.4). Mice were decapitated and the brains were removed. For acute prefrontal sections: two parallel cuts were made along the coronal plane at the rostral and caudal ends of the brains; brains were mounted on the flat surface created at the caudal end; three coronal slices (250 mm thick) were obtained using a vibrating blade microtome (VT1200S, Leica Microsystems Inc.). Dorsal hippocampal (dHPC) slices were obtained using a blocking technique described previously (Malik et al., 2015). Briefly, dHPC slices were obtained by making a blocking cut at a 45° angle from the coronal plane starting at the posterior end of the forebrain. A second blocking cut was made at 45° relative to the coronal plane, but starting from approximately one-third of the total length of the forebrain (from the most anterior point). Brains were mounted on the flat surface created by the first blocking cut. Approximately, 3 dorsal slices were obtained from each hemisphere.

Author Manuscript Author Manuscript Author Manuscript Author Manuscript

Slices were allowed to recover at 34 °C for 30 min followed by 30 min recovery at room temperature in a holding solution containing (in mM) 125 NaCl, 2.5 KCl, 1.25 NaH_2PO_4, 25 $NaHCO_3$, 2 $CaCl_2$, 2 $MgCl_2$, 12.5 dextrose, 1.3 ascorbic acid, 3 sodium pyruvate.

Ex-vivo patch clamp recordings: Somatic whole-cell current-clamp and voltage-clamp recordings were obtained as previously described (Malik and Johnston, 2017; Malik et al., 2019). Briefly, submerged slices were perfused in heated (32–34 °C) artificial cerebrospinal fluid (aCSF) containing (in mM): 125 NaCl, 3 KCl, 1.25 $NaH_2 PO_4$, 25 $NaHCO_3$, 2 $CaCl_2$, 1 $MgCl_2$, 12.5 dextrose (bubbled with 95% O_2/5% CO_2, pH ~7.4). Neurons were visualized using DIC optics (and eYFP fluorescence in a few experiments) fitted with a 40x water-immersion objective (BX51WI, Olympus microscope). During recordings from prefrontal slices, dHPC projecting PFC LRG neurons in all cortical layers were identified by eYFP expression. During recordings from hippocampal slices, CA1 pyramidal neurons (PNs) and CA1 local inhibitory neurons (INs) were identified using laminar location (under DIC optics) and intrinsic properties of the recorded neurons.

Patch electrodes (2–3 MΩ) were pulled from borosilicate capillary glass of external diameter 1 mm (Sutter Instruments) using a Flaming/Brown micropipette puller (model P-2000, Sutter Instruments). For current-clamp recordings, electrodes were filled with an internal solution containing the following (in mM): 134 K-gluconate, 6 KCl, 10 HEPES, 4 NaCl, 7 K_2-phosphocreatine, 0.3 Na-GTP, and 4 Mg-ATP (pH ~7.3 adjusted with KOH). Biocytin (Vector Laboratories) was included (0.1–0.2%) for subsequent histological processing of recipient CA1 neurons. For voltage-clamp recordings, the internal solution contained the following (in mM): 130 Csmethanesulfonate, 10 CsCl, 10 HEPES, 4 NaCl, 7 phosphocreatine, 0.3 Na-GTP, 4 Mg-ATP, and 2 QX314-Br (pH ~7.3 adjusted with CsOH). In a few recordings, 15 μm AlexaFluor-594 (Invitrogen) was also added to the internal solution. Electrophysiology data were recorded using Multiclamp 700B amplifier (Molecular Devices). Voltages have not been corrected for measured liquid junction potential (~8 mV). Data collection was started 5–8 min after successful transition to the whole-cell configuration. Series resistance and pipette capacitance were appropriately compensated before each recording. Series resistance was usually 10–20 MΩ, and experiments were terminated if series resistances exceeded 25 MΩ.

Data analysis: *Ex vivo* electrophysiology data were analyzed using custom routines written in IGOR Pro (Wavemetrics). Resting membrane potential (RMP) was measured in current-clamp mode immediately after reaching whole-cell configuration. Input resistance (Rin) was calculated as the slope of the linear fit of the voltage-current plot generated from a family of hyperpolarizing and depolarizing current injections (−50 to +20 pA, steps of 10 pA). Firing output was calculated as the number of action potentials (APs) fired in response to 800 ms long depolarizing current injections (25–500 pA). Firing frequency was calculated as the number of APs fired per second. Firing traces in response to 50 pA current above the rheobase were used for analysis of single AP properties – AP threshold, maximum dV/dt (rate of rise of AP), AP amplitude, AP half-width, and fast afterhyperpolarization (fAHP) amplitude. AP threshold was defined as the voltage at which the value of third derivative of voltage with time is maximum. Action potential amplitude was measured

Author Manuscript Author Manuscript Author Manuscript Author Manuscript

from threshold to peak, and the half-width was measured at half this distance. Fast after hyperpolarization was measured from the threshold to the negative voltage peak after the AP. Index of spike-frequency accommodation (SFA) was calculated as the ratio of the last inter-spike interval to the first inter-spike interval.

Recorded inhibitory neurons (INs) in PFC and dorsal CA1 were classified as fast spiking, regular spiking or irregular spiking based on electrophysiological properties. Specifically, INs were classified as fast spiking if they met 3 out of the 4 following criteria: AP half-width was <0.5 ms, firing frequency >50 Hz, fAHP amplitude >14 mV, and SFA index <2. Irregular spiking INs were initially visually identified based on their high variability in inter-spike interval and burst-like intermittent spiking properties. This classification was confirmed using a firing frequency threshold (<50 Hz) and/or an SFA index threshold (>2). Dorsal CA1 neurons were classified as pyramidal neurons if they satisfied the following criteria: cell body located in stratum pyramidale, AP half-width > 1 ms, fAHP amplitude <5 mV, and maximum firing frequency <20 Hz.

To measure optogenetically evoked spiking in ChR2-eYFP+ PFC INs and to measure optogenetically evoked postsynaptic currents (oPSCs) in CA1 neurons, ChR2 was stimulated using 5 ms long light pulses (maximum light power, 4 mW/mm2) generated by a Lambda DG-4 high-speed optical switch with a 300 W Xenon lamp (Sutter Instruments) and an excitation filter centered around 470 nm. Light pulses were delivered to the slice through a 40x objective (Olympus). To measure the reversal potential of oPSCs, the holding potentials were systematically varied from −100 to +20 mV in 10 mV steps. The drugs applied were 6-cyano-7-nitroquinoxaline-2,3-dione disodium salt hydrate (CNQX), 2-(3-carboxypropyl)-3-amino-6-(4 methoxyphenyl)-pyridazinium bromide (Gabazine), and d-2-amino-5-phosphonopentanoic acid (D-AP5) (Tocris). Drugs were prepared as concentrated stock solutions and were diluted in ACSF on the day of the experiment.

To measure afferent input mediated feedforward excitation and inhibition in CA1 PNs, bipolar stimulating electrodes (Microprobes) were placed in stratum radiatum (SR) and stratum lacunosum-moleculare (SLM) to stimulate Schaffer collateral (SC) and temporo ammonic (TA) inputs, respectively. The protocol for theta-burst stimulation (TBS) consisted of bursts with five electrical stimulations (40 Hz) repeated at 5 Hz. To measure the effect of PFC LRG inputs on firing output and EPSP summation during TBS protocol, train of 470 nm light pulses (20 Hz, 5 ms) was delivered through the 40x objective. Firing frequency during TBS was calculated as the average number or APs fired per burst, and summation was estimated as the area of the last EPSP in the TBS train.

In vivo Ca^{2+} imaging

Surgery: Mice underwent two stereotactic surgeries. Cre-dependent AAV5-Syn-FLEX-ChrimsonR-tdTomato virus (Addgene) was injected in PFC (1.8 AP, ±0.3 ML, −2.4 DV) of *Dlxi12b-Cre+* and Cre-negative mice. Following this, 500–550 nL of AAV9-Syn-jGCaMP7f-WPRE virus (diluted 1:2; Addgene) (Dana et al., 2019) was injected in dorsal CA1 to express synapsin-driven calcium sensor jGCaMP7f (injection coordinates: −1.4 AP, +0.8 ML, −1.5 DV). After 3–4 weeks of viral expression, cortex overlying dorsal CA1 was slowly aspirated and a 1 mm diameter x 4 mm long integrated GRIN lens (Inscopix) was

Author Manuscript Author Manuscript Author Manuscript Author Manuscript

slowly advanced above the dorsal CA1 and cemented in place with Metabond dental cement. Mice were allowed to recover for at least 3 weeks before starting behavior and imaging experiments.

Combined Ca^{2+} imaging and optogenetics: Imaging data were collected using a miniaturized one-photon microscope (nVoke2; Inscopix Inc.). GCaMP7f signals (Ca^{2+} activity) were detected using 435–460 nm excitation LED (0.1–0.2 mW), and optogenetic stimulation of ChrimR-expressing axons was performed using a second excitation LED centered around 590–650 nm (5 ms pulses at 20 Hz, 1–2 mW light power). Ca^{2+} movies were acquired at 20 frames per second, spatially downsampled (4x), and were stored for offline data processing.

Mice were placed into a large housing cage (48 3 35 cm) for 2–3 days for 20 min where they habituated to the scope. After habituation, mice underwent a two-day behavioral testing protocol for recording NOE related Ca^{2+} activity in CA1 neurons. On day 1, mice were allowed to explore the large home cage for 15 min (HC epoch). Following this, mice were allowed to explore a novel object introduced in the cage for 15 min (NOE epoch). On day 2, mice were allowed to explore the home cage for 15 min (HC epoch) followed by optogenetic stimulation during home cage exploration for 10 min (HC + LRG stim epoch). Mice were then allowed to explore a novel object combined with optogenetic stimulation of PFC–dHPC LRG projections (NOE + LRG stim epoch). The behavior of mice during different epochs was recorded using ANY-maze software, and input TTL pulses from a computer running ANY-maze software to the data acquisition computer running nVoke2 acquisition software were used to synchronize Ca^{2+} imaging and mouse behavior movies.

Data analysis: Ca^{2+} imaging movies were preprocessed using Inscopix Data Processing Software (IDPS; Inscopix, Inc.). The video frames were spatially filtered (band-pass) with cut-offs set to 0.005 pixel-1 (low) and 0.5 pixel-1 (high) followed by frame-by-frame motion correction for removing movement artifacts associated with respiration and head-unrestrained behavior. The mean image over the imaging session was computed, and the dF/F was computed using this mean image. The resultant preprocessed movies were then exported into MATLAB, and cell segmentation was performed using an open-source calcium imaging software (CIAPKG) (Corder et al., 2019). Specifically, we used a Principal Component Analysis/Independent Component Analysis (PCA/ICA) approach to detect and extract ROIs (presumed neurons) per field of view (Mukamel et al., 2009). For each movie, the extracted output neurons were then manually sorted to remove overlapping neurons, neurons with low SNR, and neurons with aberrant shapes.

Accepted neurons and their Ca^{2+} activity traces were exported to MATLAB for further analysis using custom scripts (as previously described in (Frost et al., 2021)). Briefly, we calculated the standard deviation (σ) of the Ca^{2+} movie and used this to perform threshold-based event detection on the traces by first detecting increases in dF/F exceeding 2σ (over one second). Subsequently, we detected events that exceeded 10σ for over two seconds and had a total area under the curve higher than 150σ. The peak of the event was estimated as the local maximum of the entire event. For an extracted output neuron, active frames were

Author Manuscript Author Manuscript Author Manuscript Author Manuscript

marked as the period from the beginning of an event until the Ca^{2+} signal decreased 30% from the peak of the event (up to a maximum of 2 s).

Procedure for measuring object-related changes in Ca^{2+} activity: Frame-by-frame x-y positions of the head of a mouse in the testing cage were detected using DeepLabCut. A small rectangular area surrounding the object location in the testing cage was marked as the object zone. Time points (frames acquired at 30 Hz and resampled at 20 Hz, using resample function in MATLAB) when the mouse's head was inside the object zone were classified as INbin and the remaining frames were classified as OUTbin. We then recorded the frame-by-frame Ca^{2+} activity of neurons corresponding to the INbin and OUTbin position frames. For all extracted neurons, the mean activity for INbin (μ_{INbin}) and OUTbin (μ_{OUTbin}) frames were calculated. We also calculated the standard deviation (SD_{OUTbin}) of neuronal activity in OUTbin frames. The z-scored activity of each neuron was estimated using Equation 2.1. The object signal-to-noise ratio (Object SNR) was calculated using the z-scored activity during HC and NOE epochs (Equation 2.2).

$$zscore = \frac{\mu_{INbin} - \mu_{OUTbin}}{SD_{OUTbin}} \quad \text{(Equation 2.1)}$$

$$Object\ SNR = zscore_{NOE} - Zscore_{HC} \quad \text{(Equation 2.2)}$$

Control location SNR was calculated similarly using the positions of the mouse inside and outside three non-overlapping control locations.

Registration of cells across imaging sessions: To compare activity of CA1 neurons during NOE sessions on day 1 and day 2, cells were tracked across sessions using CellReg (Sheintuch et al., 2017). Briefly, rigid alignment with both translations and rotations was performed on spatial ROI footprints of each session and manually inspected for quality. Identities of the registered cells (i.e. cells tracked across both recording days) were used for pairwise comparisons presented in Figure S6.

Place field analysis—Place field analysis was performed in MATLAB using custom scripts and previously published analysis scripts (https://github.com/SharpWave/PlacefieldAnalysis) (Kinsky et al., 2018). Calcium imaging and mouse position data during the imaging sessions was speed filtered to exclude time periods with running speeds below 1 cm/s. Data from different epochs (i.e., HC and NOE on day 1 and day 2) were analyzed separately. Rate maps were constructed by summing the total number of Ca^{2+} events that occurred in a location bin (2.5 × 2.5 cm) divided by the total occupancy time of the mouse in that bin. The rate maps were then smoothed with a Gaussian kernel (σ = 2.5cm). Place fields were defined as all connected occupancy bins whose smoothed event rate exceeded 50% of the peak event rate. If a neuron had multiple place fields, the size and location of the its largest place field was used for analysis.

Spatial information content was calculated as previously described (Skaggs et al., 1993) (Equation 3.1).

Author Manuscript Author Manuscript Author Manuscript Author Manuscript

$$Spatial\ Information = \sum_i P_i \frac{R_i}{R} \log_2 \frac{R_i}{R} \quad \text{(Equation 3.1)}$$

where i is the bin number, P_i is the probability of occupancy for bin i, R_i is the calcium event rate for bin i, and R is the overall calcium event rate. To determine whether CA1 neurons had above chance spatial selectivity (i.e., place cells vs. non-place cells), we first calculated the spatial information content for each neuron. Then we circularly shuffled the entire sequence of calcium activity for every neuron 500 times and calculated the spatial information for the shuffled activity raster. Specifically, the end of the activity raster was circularly wrapped to the start by a random interval ranging between 20 s and session duration − 20s. A neuron was classified as a place cell if its spatial information content was above 80% percentile of the shuffled distribution of that neuron (Meshulam et al., 2017).

To measure the relative proportion of the recording cage on which the neurons were active, we calculated the sparsity index as described by (Jung et al., 1994) (Equation 3.2).

$$Sparsity\ index = \sum_i (P_i * R_i)^2 / R^2 \quad \text{(Equation 3.2)}$$

Additional spatial properties compared include the peak and mean in-field and out-field firing rates, number of place fields, and size of largest place field. For remapping analysis, distance between the largest PF centroid during HC epoch and largest PF centroid during NOE epoch were calculated for every neuron. Correlations between this remapping distance and the PF centroid distance from the object in the NOE epoch of all imaged neurons were analyzed and are shown in Figure 7.

Histological processing

Assessment of virus expression and anterograde tracing of LRG projections: Animals were transcardially perfused with PBS, and then with 4% paraformaldehyde (PFA). The brains were post-fixed for at least one day in PFA solution. Coronal sections (50–75 μm thick) were obtained using a vibratome. Sections that included the injection sites, electrode implantation sites and lens implantation sites were mounted on slides and cover-slipped using a glycerol-base, aqueous mounting medium (Vectashield Plus Antifade Mounting Medium, Vector labs). Sections were first scanned using an upright wide-field fluorescence microscope. Following this, confocal images were taken with 10x and 20x objectives on an Andor Borealis CSU-W1 spinning disk confocal mounted on a Nikon Ti Microscope (UCSF Nikon Imaging Center, NIH S10 Shared Instrumentation grant 1S10OD017993–01A1) and captured with an Andor Zyla sCMOS camera and Micro-Manager software (Open Imaging).

Inhibitory neuron marker expression in recipient CA1 neurons: Slices containing biocytin-filled cells were fixed overnight in a buffered solution containing 4% PFA. Slices were rinsed in PBS, then blocked and permeabilized in PBS with 5% Donkey Serum, 0.3% Triton X-100 and 1% BSA. Slices were immuno-stained overnight with one or two primary antibodies: rabbit anti-PV (Swant; diluted 1:200), rat anti-SST (Millipore, diluted 1:200), or rabbit anti-VIP (Immunostar, diluted 1:200). Slices were washed 6 × 10min in PBS

Author Manuscript Author Manuscript Author Manuscript Author Manuscript

containing 0.3% Triton X-100. Slices were incubated with donkey anti-rabbit Alexa-488, donkey anti-rat Alexa 594 secondary antibody (1:800, Thermo Fisher), and Streptavidin-647 (1:300, Thermo Fisher) overnight at 4°C. After washing 6 × 10min in PBS with 0.3% Triton X-100, slices were mounted with an aqueous mounting medium. Confocal mages were obtained as described above.

Inhibitory neuron (IN) marker expression in CTb tagged PFC LRG neurons: 5–7 days after CTb injection, mice were transcardially perfused with PBS followed by 4% PFA solution, and brains were post-fixed for at least one day. Coronal sections (75 mm) were obtained using a vibratome, and immuhistochemistry was performed (as described above). The following primary antibodies were used to stain for IN markers: rabbit anti-PV (Swant; diluted 1:200); rat anti-SST (Millipore, diluted 1:200); rabbit anti-VIP (Immunostar, diluted 1:200); rabbit anti-NPY (Immunostar, diluted 1:500); rabbit anti-calretinin (Immunostar, diluted 1:500); rabbit anti-nNOS (Life technologies, diluted 1:500), and goat anti-CTb (List, diluted 1:500). The following secondary antibodies were used: donkey anti-rabbit Alexa 488; donkey anti-rat Alexa 488; and donkey anti-goat Alexa 594. For each IN marker, confocal images collected from mounted sections were used to manually count the number of CTb+ and IN marker+ PFC neurons (ImageJ software).

Analysis of axon collaterals: SST-Cre, PV-Cre, and VIP-Cre mice received unilateral injections of 1:2 diluted AAV8-CON/FON-eYFP virus (Addgene) (Fenno et al., 2014) into the PFC and AAVretrograde-EF1a-Flpo (Addgene) into the dHPC. After waiting 7–8 weeks for sufficient expression, mice were transcardially perfused with PBS and PFA, and brains were post-fixed for at least one day. Coronal sections (75 mm thick) were obtained using a vibratome and mounted on slides and cover-slipped using Vectashield Plus Antifade Mounting Medium (Vector labs). Sections were imaged using an upright wide-field fluorescence microscope (BZ-X series fluorescence microscope, KEYENCE). A small cohort of control mice received AAV8-CON/FON-eYFP virus injections into the PFC. Sections from these mice lacked eYFP expression (data not shown) suggesting that the injected titer of AAV8-CON/FON-eYFP virus does not lead to Cre and Flp independent eYFP expression.

QUANTIFICATION AND STATISTICAL ANALYSIS

Detailed statistical analyses were performed using MATLAB and Graphpad Prism. Comparisons of means were performed using paired or unpaired two-tailed Student's *t* test, one-way ANOVA or two-way repeated measures ANOVA with Tukey post hoc test unless otherwise stated. For non-parametric data sets, we used Chi-square, Wilcoxon rank sum, and Friedman tests to determine significance. Sample sizes and statistical tests and parameters are listed in the figure legends. Data are reported as mean ± S.E.M. unless otherwise stated.

Supplementary Material

Refer to Web version on PubMed Central for supplementary material.

Author Manuscript Author Manuscript Author Manuscript Author Manuscript

ACKNOWLEDGMENTS

We thank Madhur Sharma and Helia Seifikar for technical support. We are grateful to Loren Frank, Mazen Kheirbek, Nicholas Frost, Adam Jackson, and Max Ladow for comments on earlier versions of this manuscript. This work was supported by National Institute of Mental Health (R01MH106507 and R01MH117961 to V.S.S.) and 2018 NARSAD Young Investigator Grant from Brain & Behavior Research Foundation (Leichtung Family investigator, R.M.). Confocal images were acquired at the Nikon Imaging Center at the University of California, San Francisco.

REFERENCES

Acsády L, Arabadzisz D, and Freund TF (1996a). Correlated morphological and neurochemical features identify different subsets of vasoactive intestinal polypeptide-immunoreactive interneurons in rat hippocampus. Neuroscience 73, 299–315. 10.1016/0306-4522(95)00610-9. [PubMed: 8783251]

Acsády L, Görcs TJ, and Freund TF (1996b). Different populations of vasoactive intestinal polypeptide-immunoreactive interneurons are specialized to control pyramidal cells or interneurons in the hippocampus. Neuroscience 73, 317–334. 10.1016/0306-4522(95)00609-5. [PubMed: 8783252]

Anderson MC, Bunce JG, and Barbas H. (2016). Prefrontal-hippocampal pathways underlying inhibitory control over memory. Neurobiol. Learn. Mem 134, 145–161. 10.1016/j.nlm.2015.11.008. [PubMed: 26642918]

Ang CW, Carlson GC, and Coulter DA (2005). Hippocampal CA1 circuitry dynamically gates direct cortical inputs preferentially at theta frequencies. J. Neurosci 25, 9567–9580. 10.1523/jneurosci.2992-05.2005. [PubMed: 16237162]

Barker GRI, Bird F, Alexander V, and Warburton EC (2007). Recognition memory for objects, place, and temporal order: a disconnection analysis of the role of the medial prefrontal cortex and perirhinal cortex. J. Neurosci 27, 2948– 2957. 10.1523/jneurosci.5289-06.2007. [PubMed: 17360918]

Basu J, Zaremba JD, Cheung SK, Hitti FL, Zemelman BV, Losonczy A, and Siegelbaum SA (2016). Gating of hippocampal activity, plasticity, and memory by entorhinal cortex long-range inhibition. Science 351, aaa5694. 10.1126/science.aaa5694.

Bähner F, Demanuele C, Schweiger J, Gerchen MF, Zamoscik V, Ueltzhöffer K, Hahn T, Meyer P, Flor H, Durstewitz D, et al. (2015). Hippocampal-dorsolateral prefrontal coupling as a species-conserved cognitive mechanism: a human translational imaging study. Neuropsychopharmacology 40, 1674–1681. 10.1038/npp.2015.13. [PubMed: 25578799]

Bittner KC, Grienberger C, Vaidya SP, Milstein AD, Macklin JJ, Suh J, Tonegawa S, and Magee JC (2015). Conjunctive input processing drives feature selectivity in hippocampal CA1 neurons. Nat. Neurosci 18, 1133–1142. 10.1038/nn.4062. [PubMed: 26167906]

Bourboulou R, Marti G, Michon F-X, El Feghaly E, Nouguier M, Robbe D, Koenig J, and Epsztein J. (2019). Dynamic control of hippocampal spatial coding resolution by local visual cues. eLife 8, e44487. 10.7554/elife.44487. [PubMed: 30822270]

Brincat SL, and Miller EK (2015). Frequency-specific hippocampal-prefrontal interactions during associative learning. Nat. Neurosci 18, 576–581. 10.1038/nn.3954. [PubMed: 25706471]

Burke SN, Maurer AP, Nematollahi S, Uprety AR, Wallace JL, and Barnes CA (2011). The influence of objects on place field expression and size in distal hippocampal CA1. Hippocampus 21, 783–801. 10.1002/hipo.20929. [PubMed: 21365714]

Chamberland S, and Topolnik L. (2012). Inhibitory control of hippocampal inhibitory neurons. Front. Neurosci 6, 165. 10.3389/fnins.2012.00165. [PubMed: 23162426]

Cho KKA, Davidson TJ, Bouvier G, Marshall JD, Schnitzer MJ, and Sohal VS (2020). Cross-hemispheric gamma synchrony between prefrontal parvalbumin interneurons supports behavioral adaptation during rule shift learning. Nat. Neurosci 23, 892–902. 10.1038/s41593-020-0647-1. [PubMed: 32451483]

Christenson Wick Z, Tetzlaff MR, and Krook-Magnuson E. (2019). Novel long-range inhibitory nNOS-expressing hippocampal cells. eLife 8, e46816. 10.7554/elife.46816. [PubMed: 31609204]

Author Manuscript Author Manuscript Author Manuscript Author Manuscript

Churchwell JC, Morris AM, Musso ND, and Kesner RP (2010). Prefrontal and hippocampal contributions to encoding and retrieval of spatial memory. Neurobiol. Learn. Mem 93, 415–421. 10.1016/j.nlm.2009.12.008. [PubMed: 20074655]

Colgin LL (2011). Oscillations and hippocampal–prefrontal synchrony. Curr. Opin. Neurobiol 21, 467–474. 10.1016/j.conb.2011.04.006. [PubMed: 21571522]

Corder G, Ahanonu B, Grewe BF, Wang D, Schnitzer MJ, and Scherrer G. (2019). An amygdalar neural ensemble that encodes the unpleasantness of pain. Science 363, 276–281. 10.1126/science.aap8586. [PubMed: 30655440]

Csicsvari J, Jamieson B, Wise KD, and Buzsáki G. (2003). Mechanisms of gamma oscillations in the Hippocampus of the behaving rat. Neuron 37, 311–322. 10.1016/s0896-6273(02)01169-8. [PubMed: 12546825]

Cunniff MM, Markenscoff-Papadimitriou E, Ostrowski J, Rubenstein JL, and Sohal VS (2020). Altered hippocampal-prefrontal communication during anxiety-related avoidance in mice deficient for the autism-associated gene Pogz. eLife 9, e54835. 10.7554/elife.54835. [PubMed: 33155545]

Dana H, Sun Y, Mohar B, Hulse BK, Kerlin AM, Hasseman JP, Tsegaye G, Tsang A, Wong A, Patel R, et al. (2019). High-performance calcium sensors for imaging activity in neuronal populations and microcompartments. Nat. Meth 16, 649–657. 10.1038/s41592-019-0435-6.

del Rio D, Beucher B, Lavigne M, Wehbi A, Gonzalez Dopeso-Reyes I, Saggio I, and Kremer EJ (2019). CAV-2 vector development and gene transfer in the central and peripheral nervous Systems. Front. Mol. Neurosci 12, 71. 10.3389/fnmol.2019.00071. [PubMed: 30983967]

DeVito LM, and Eichenbaum H. (2010). Distinct contributions of the hippocampus and medial prefrontal cortex to the “what-where-when” components of episodic-like memory in mice. Behav. Brain Res 215, 318–325. 10.1016/j.bbr.2009.09.014. [PubMed: 19766146]

Eichenbaum H. (2017). Prefrontal–hippocampal interactions in episodic memory. Nat. Rev. Neurosci 18, 547–558. 10.1038/nrn.2017.74. [PubMed: 28655882]

Fenno LE, Mattis J, Ramakrishnan C, Hyun M, Lee SY, He M, Tucciarone J, Selimbeyoglu A, Berndt A, Grosenick L, et al. (2014). Targeting cells with single vectors using multiple-feature Boolean logic. Nat. Meth 11, 763–772. 10.1038/nmeth.2996.

Floresco SB, Seamans JK, and Phillips AG (1997). Selective roles for hippocampal, prefrontal cortical, and ventral striatal circuits in radial-arm maze tasks with or without a delay. J. Neurosci 17, 1880–1890. 10.1523/jneurosci.17-05-01880.1997. [PubMed: 9030646]

Francavilla R, Villette V, Luo X, Chamberland S, Muňoz-Pino E, Camiré O, Wagner K, Kis V, Somogyi P, and Topolnik L. (2018). Connectivity and network state-dependent recruitment of long-range VIP-GABAergic neurons in the mouse hippocampus. Nat. Commun 9, 5043. 10.1038/s41467-018-07162-5. [PubMed: 30487571]

Freund TF, and Buzsaki G. (1996). Interneurons of the hippocampus. Hippocampus 6, 347–470. 10.1002/(sici)1098-1063(1996)6:4<347::aidhipo1>3.0.co;2-i. [PubMed: 8915675]

Frost NA, Haggart A, and Sohal VS (2021). Dynamic patterns of correlated activity in the prefrontal cortex encode information about social behavior. PLoS Biol. 19, e3001235EP. 10.1371/journal.pbio.3001235.

Gazzaley A, and D’Esposito M. (2007). Unifying prefrontal cortex function: executive control, neural networks, and top-down modulation. In The Human Frontal Lobes: Functions and Disorders, Second edition, Miller BL and Cumming JL, eds. (The Guilford Press), pp. 187–206.

Godsil BP, Kiss JP, Spedding M, and Jay TM (2013). The hippocampal-prefrontal pathway: the weak link in psychiatric disorders? Eur. Neuropsychopharmacol 23, 1165–1181. 10.1016/j.euroneuro.2012.10.018. [PubMed: 23332457]

Grienberger C, Milstein AD, Bittner KC, Romani S, and Magee JC (2017). Inhibitory suppression of heterogeneously tuned excitation enhances spatial coding in CA1 place cells. Nat. Neurosci 20, 417–426. 10.1038/nn.4486. [PubMed: 28114296]

Guise KG, and Shapiro ML (2017). Medial prefrontal cortex reduces memory interference by modifying hippocampal encoding. Neuron 94, 183–192.e8. 10.1016/j.neuron.2017.03.011.e188. [PubMed: 28343868]

Author Manuscript Author Manuscript Author Manuscript Author Manuscript

Hallock HL, Wang A, and Griffin AL (2016). Ventral midline thalamus is critical for hippocampal-prefrontal synchrony and spatial working memory. J. Neurosci 36, 8372–8389. 10.1523/jneurosci.0991-16.2016. [PubMed: 27511010]

Hnasko TS, Perez FA, Scouras AD, Stoll EA, Gale SD, Luquet S, Phillips PEM, Kremer EJ, and Palmiter RD (2006). Cre recombinase-mediated restoration of nigrostriatal dopamine in dopamine-deficient mice reverses hypophagia and bradykinesia. Proc. Natl. Acad. Sci. U S A 103, 8858–8863. 10.1073/pnas.0603081103. [PubMed: 16723393]

Hoover WB, and Vertes RP (2007). Anatomical analysis of afferent projections to the medial prefrontal cortex in the rat. Brain Struct. Funct 212, 149–179. 10.1007/s00429-007-0150-4. [PubMed: 17717690]

Hoover WB, and Vertes RP (2012). Collateral projections from nucleus reuniens of thalamus to hippocampus and medial prefrontal cortex in the rat: a single and double retrograde fluorescent labeling study. Brain Struct Funct 217, 191–209. [PubMed: 21918815]

Jay TM, and Witter MP (1991). Distribution of hippocampal CA1 and subicular efferents in the prefrontal cortex of the rat studied by means of anterograde transport of Phaseolus vulgaris-leucoagglutinin. J. Comp. Neurol 313, 574–586. 10.1002/cne.903130404. [PubMed: 1783682]

Jin J, and Maren S. (2015). Prefrontal-hippocampal interactions in memory and emotion. Front. Syst. Neurosci 9, 1082. 10.3389/fnsys.2015.00170.

Jinno S, Klausberger T, Marton LF, Dalezios Y, Roberts JDB, Fuentealba P, Bushong EA, Henze D, Buzsaki G, and Somogyi P. (2007). Neuronal diversity in GABAergic long-range projections from the Hippocampus. J. Neurosci 27, 8790–8804. 10.1523/jneurosci.1847-07.2007. [PubMed: 17699661]

Jones MW, and Wilson MA (2005). Theta rhythms coordinate hippocampal-prefrontal interactions in a spatial memory task. PLoS Biol. 3, e402. 10.1371/journal.pbio.0030402. [PubMed: 16279838]

Jung MW, Wiener SI, and McNaughton BL (1994). Comparison of spatial firing characteristics of units in dorsal and ventral hippocampus of the rat. J. Neurosci 14, 7347–7356. 10.1523/jneurosci.14-12-07347.1994. [PubMed: 7996180]

Kinsky NR, Sullivan DW, Mau W, Hasselmo ME, and Eichenbaum HB (2018). Hippocampal place fields maintain a coherent and flexible map across long timescales. Curr. Biol 28, 3578–3588.e6. 10.1016/j.cub.2018.09.037.e6. [PubMed: 30393037]

Klapoetke NC, Murata Y, Kim SS, Pulver SR, Birdsey-Benson A, Cho YK, Morimoto TK, Chuong AS, Carpenter EJ, Tian Z, et al. (2014). Independent optical excitation of distinct neural populations. Nat. Meth 11, 338–346. 10.1038/nmeth.2836.

Knierim JJ (2002). Dynamic interactions between local surface cues, distal landmarks, and intrinsic circuitry in hippocampal place cells. J. Neurosci 22, 6254–6264. 10.1523/jneurosci.22-14-06254.2002. [PubMed: 12122084]

Kupferschmidt DA, and Gordon JA (2018). The dynamics of disordered dialogue: prefrontal, hippocampal and thalamic miscommunication underlying working memory deficits in schizophrenia. Brain Neurosci. Adv 2. 239821281877182. 10.1177/2398212818771821.

Kyd RJ, and Bilkey DK (2003). Prefrontal cortex lesions modify the spatial properties of hippocampal place cells. Cereb. Cortex 13, 444–451. 10.1093/cercor/13.5.444. [PubMed: 12679291]

Lee AT, Cunniff MM, See JZ, Wilke SA, Luongo FJ, Ellwood IT, Ponnavolu S, and Sohal VS (2019). VIP interneurons contribute to avoidance behavior by regulating information flow across hippocampal-prefrontal networks. Neuron 102, 1223–1234.e4. 10.1016/j.neuron.2019.04.001.e1224. [PubMed: 31053407]

Lee AT, Vogt D, Rubenstein JL, and Sohal VS (2014). A class of GABAergic neurons in the prefrontal cortex sends long-range projections to the nucleus accumbens and elicits acute avoidance behavior. J. Neurosci 34, 11519–11525. 10.1523/jneurosci.1157-14.2014. [PubMed: 25164650]

Li M, Long C, and Yang L. (2015). Hippocampal-prefrontal circuit and disrupted functional connectivity in psychiatric and neurodegenerative disorders. Biomed. Res. Int 2015, 1–10. 10.1155/2015/810548.

Malik R, and Johnston D. (2017). Dendritic GIRK channels gate the integration window, plateau potentials, and induction of synaptic plasticity in dorsal but not ventral CA1 neurons. J. Neurosci 37, 3940–3955. 10.1523/jneurosci.2784-16.2017. [PubMed: 28280255]

Author Manuscript Author Manuscript Author Manuscript Author Manuscript

Malik R, Dougherty KA, Parikh K, Byrne C, and Johnston D. (2015). Mapping the electrophysiological and morphological properties of CA1 pyramidal neurons along the longitudinal hippocampal axis. Hippocampus 26, 341–361. 10.1002/hipo.22526. [PubMed: 26333017]

Malik R, Pai EL-L, Rubin AN, Stafford AM, Angara K, Minasi P, Rubenstein JL, Sohal VS, and Vogt D. (2019). Tsc1 represses parvalbumin expression and fast-spiking properties in somatostatin lineage cortical interneurons. Nat. Commun 10, 4994–5016. 10.1038/s41467-019-12962-4. [PubMed: 31676823]

Mathis A, Mamidanna P, Cury KM, Abe T, Murthy VN, Mathis MW, and Bethge M. (2018). DeepLabCut: markerless pose estimation of userdefined body parts with deep learning. Nat. Neurosci 21, 1281–1289. 10.1038/s41593-018-0209-y. [PubMed: 30127430]

Mattis J, Tye KM, Ferenczi EA, Ramakrishnan C, O'Shea DJ, Prakash R, Gunaydin LA, Hyun M, Fenno LE, Gradinaru V, et al. (2012). Principles for applying optogenetic tools derived from direct comparative analysis of microbial opsins. Nat. Meth 9, 159–172. 10.1038/nmeth.1808.

Melzer S, and Monyer H. (2020). Diversity and function of corticopetal and corticofugal GABAergic projection neurons. Nat. Rev. Neurosci 21, 499–515. 10.1038/s41583-020-0344-9. [PubMed: 32747763]

Melzer S, Michael M, Caputi A, Eliava M, Fuchs EC, Whittington MA, and Monyer H. (2012). Long-range-projecting GABAergic neurons modulate inhibition in hippocampus and entorhinal cortex. Science 335, 1506–1510. 10.1126/science.1217139. [PubMed: 22442486]

Meshulam L, Gauthier JL, Brody CD, Tank DW, and Bialek W. (2017). Collective behavior of place and non-place neurons in the hippocampal network. Neuron 96, 1178–1191.e4. 10.1016/j.neuron.2017.10.027.e4. [PubMed: 29154129]

Miller EK, and Cohen JD (2001). An integrative theory of prefrontal cortex function. Annu. Rev. Neurosci 24, 167–202. 10.1146/annurev.neuro.24.1.167. [PubMed: 11283309]

Miller EK (2000). The prefontral cortex and cognitive control. Nat. Rev. Neurosci 1, 59–65. 10.1038/35036228. [PubMed: 11252769]

Milstein AD, Bloss EB, Apostolides PF, Vaidya SP, Dilly GA, Zemelman BV, and Magee JC (2015). Inhibitory gating of input comparison in the CA1 microcircuit. Neuron 87, 1274–1289. 10.1016/j.neuron.2015.08.025. [PubMed: 26402609]

Moser EI, Kropff E, and Moser M-B (2008). Place cells, grid cells, and the brain's spatial representation system. Annu. Rev. Neurosci 31, 69–89. 10.1146/annurev.neuro.31.061307.090723. [PubMed: 18284371]

Mukamel EA, Nimmerjahn A, and Schnitzer MJ (2009). Automated analysis of cellular signals from large-scale calcium imaging data. Neuron 63, 747–760. 10.1016/j.neuron.2009.08.009. [PubMed: 19778505]

O'Keefe J. (1976). Place units in the hippocampus of the freely moving rat. Exp. Neurol 51, 78–109. 10.1016/0014-4886(76)90055-8. [PubMed: 1261644]

O'Keefe J, and Krupic J. (2021). Do hippocampal pyramidal cells respond to nonspatial stimuli? Physiol. Rev 101, 1427–1456. 10.1152/physrev.00014.2020. [PubMed: 33591856]

O'Neill P-K, Gordon JA, and Sigurdsson T. (2013). Theta oscillations in the medial prefrontal cortex are modulated by spatial working memory and synchronize with the hippocampus through its ventral subregion. J. Neurosci 33, 14211–14224. 10.1523/jneurosci.2378-13.2013. [PubMed: 23986255]

Pelkey KA, Chittajallu R, Craig MT, Tricoire L, Wester JC, and McBain CJ (2017). Hippocampal GABAergic inhibitory interneurons. Physiol. Rev 97, 1619–1747. 10.1152/physrev.00007.2017. [PubMed: 28954853]

Place R, Farovik A, Brockmann M, and Eichenbaum H. (2016). Bidirectional prefrontal-hippocampal interactions support context-guided memory. Nat. Neurosci 19, 992–994. 10.1038/nn.4327. [PubMed: 27322417]

Potter GB, Petryniak MA, Shevchenko E, McKinsey GL, Ekker M, and Rubenstein JLR (2009). Generation of Cre-transgenic mice using Dlx1/Dlx2 enhancers and their characterization in GABAergic interneurons. Mol. Cell. Neurosci 40, 167–186. 10.1016/j.mcn.2008.10.003. [PubMed: 19026749]

Author Manuscript Author Manuscript Author Manuscript Author Manuscript

Preston AR, and Eichenbaum H. (2013). Interplay of hippocampus and prefrontal cortex in memory. Curr. Biol 23, R764–R773. 10.1016/j.cub.2013.05.041. [PubMed: 24028960]

Rajasethupathy P, Sankaran S, Marshel JH, Kim CK, Ferenczi E, Lee SY, Berndt A, Ramakrishnan C, Jaffe A, Lo M, et al. (2015). Projections from neocortex mediate top-down control of memory retrieval. Nature 526, 653–659. 10.1038/nature15389. [PubMed: 26436451]

Scheggia D, Managò F, Maltese F, Bruni S, Nigro M, Dautan D, Latuske P, Contarini G, Gomez-Gonzalo M, Requie LM, et al. (2020). Somatostatin interneurons in the prefrontal cortex control affective state discrimination in mice. Nat. Neurosci 23, 47–60. 10.1038/s41593-019-0551-8. [PubMed: 31844317]

Sheintuch L, Rubin A, Brande-Eilat N, Geva N, Sadeh N, Pinchasof O, and Ziv Y. (2017). Tracking the same neurons across multiple days in Ca2+ imaging data. Cell Rep 21, 1102–1115. [PubMed: 29069591]

Shin JD, and Jadhav SP (2016). Multiple modes of hippocampal–prefrontal interactions in memory-guided behavior. Syst. Neurosci 40, 161–169. 10.1016/j.conb.2016.07.015.

Sigurdsson T, and Duvarci S. (2016). Hippocampal-prefrontal interactions in cognition, behavior and psychiatric disease. Front. Syst. Neurosci 9, 190. 10.3389/fnsys.2015.00190. [PubMed: 26858612]

Sigurdsson T, Stark KL, Karayiorgou M, Gogos JA, and Gordon JA (2010). Impaired hippocampal–prefrontal synchrony in a genetic mouse model of schizophrenia. Nature 464, 763–767. 10.1038/nature08855. [PubMed: 20360742]

Skaggs WE, McNaughton BL, Gothard KM, and Markus EJ (1993). An information-theoretic approach to deciphering the hippocampal code. Adv. Neural Inf. Process. Syst, 1030–1037.

Spellman T, Rigotti M, Ahmari SE, Fusi S, Gogos JA, and Gordon JA (2015). Hippocampal-prefrontal input supports spatial encoding in working memory. Nature 522, 309–314. 10.1038/nature14445. [PubMed: 26053122]

Stamatakis AM, Schachter MJ, Gulati S, Zitelli KT, Malanowski S, Tajik A, Fritz C, Trulson M, and Otte SL (2018). Simultaneous optogenetics and cellular resolution calcium imaging during active behavior using a miniaturized microscope 12, 496. 10.3389/fnins.2018.00496.

Stefanini F, Kushnir L, Jimenez JC, Jennings JH, Woods NI, Stuber GD, Kheirbek MA, Hen R, and Fusi S. (2020). A distributed neural code in the dentate gyrus and in CA1. Neuron 107, 703–716.e4. 10.1016/j.neuron.2020.05.022.e704. [PubMed: 32521223]

Tamamaki N, and Tomioka R. (2010). Long-range GABAergic connections distributed throughout the neocortex and their possible function. Front. Neurosci 4, 202. 10.3389/fnins.2010.00202. [PubMed: 21151790]

Trimper JB, Galloway CR, Jones AC, Mandi K, and Manns JR (2017). Gamma oscillations in rat hippocampal subregions dentate gyrus, CA3, CA1, and subiculum underlie associative memory encoding. Cell Rep. 21, 2419–2432. 10.1016/j.celrep.2017.10.123. [PubMed: 29186681]

Tukker JJ, Fuentealba P, Hartwich K, Somogyi P, and Klausberger T. (2007). Cell type-specific tuning of hippocampal interneuron firing during gamma oscillations *in vivo*. J. Neurosci 27, 8184–8189. 10.1523/jneurosci.1685-07.2007. [PubMed: 17670965]

Turi GF, Li W-K, Chavlis S, Pandi I, O'Hare J, Priestley JB, Grosmark AD, Liao Z, Ladow M, Zhang JF, et al. (2019). Vasoactive intestinal polypeptide-expressing interneurons in the Hippocampus support goal-oriented spatial learning. Neuron 101, 1150–1165.e8. 10.1016/j.neuron.2019.01.009.e1158. [PubMed: 30713030]

Varela C, Kumar S, Yang JY, and Wilson MA (2014). Anatomical substrates for direct interactions between hippocampus, medial prefrontal cortex, and the thalamic nucleus reuniens. Brain Struct Funct 219, 911–929. [PubMed: 23571778]

Vertes RP, Hoover WB, Szigeti-Buck K, and Leranth C. (2007). Nucleus reuniens of the midline thalamus: link between the medial prefrontal cortex and the hippocampus. Brain Res. Bull 71, 601–609. 10.1016/j.brainresbull.2006.12.002. [PubMed: 17292803]

Vinck M, Oostenveld R, van Wingerden M, Battaglia F, and Pennartz CMA (2011). An improved index of phase-synchronization for electrophysiological data in the presence of volume-conduction, noise and sample-size bias. Neuroimage 55, 1548–1565. 10.1016/j.neuroimage.2011.01.055. [PubMed: 21276857]

Author Manuscript Author Manuscript Author Manuscript Author Manuscript

Wang G-W, and Cai J-X (2006). Disconnection of the hippocampal-prefrontal cortical circuits impairs spatial working memory performance in rats. Behav. Brain Res 175, 329–336. 10.1016/j.bbr.2006.09.002. [PubMed: 17045348]

Warburton EC, and Brown MW (2015). Neural circuitry for rat recognition memory. Behav. Brain Res 285, 131–139. 10.1016/j.bbr.2014.09.050. [PubMed: 25315129]

Wiegert JS, Mahn M, Prigge M, Printz Y, and Yizhar O. (2017). Silencing neurons: tools, applications, and experimental constraints. Neuron 95, 504–529. 10.1016/j.neuron.2017.06.050. [PubMed: 28772120]

Wilson MA, and McNaughton BL (1993). Dynamics of the hippocampal ensemble code for space. Science 261, 1055–1058. 10.1126/science.8351520. [PubMed: 8351520]

Xu W, and Südhof TC (2013). A neural circuit for memory specificity and generalization. Science 339, 1290–1295. 10.1126/science.1229534. [PubMed: 23493706]

Yizhar O, Fenno LE, Prigge M, Schneider F, Davidson TJ, O'Shea DJ, Sohal VS, Goshen I, Finkelstein J, Paz JT, et al. (2011). Neocortical excitation/inhibition balance in information processing and social dysfunction. Nature 477, 171–178. 10.1038/nature10360. [PubMed: 21796121]

Yoon T, Okada J, Jung MW, and Kim JJ (2008). Prefrontal cortex and hippocampus subserve different components of working memory in rats. Learn. Mem 15, 97–105. 10.1101/lm.850808. [PubMed: 18285468]

Yu JY, and Frank LM (2015). Hippocampal-cortical interaction in decision making. Neurobiol. Learn. Mem 117, 34–41. 10.1016/j.nlm.2014.02.002. [PubMed: 24530374]

Ziv Y, Burns LD, Cocker ED, Hamel EO, Ghosh KK, Kitch LJ, Gamal AE, and Schnitzer MJ (2013). Long-term dynamics of CA1 hippocampal place codes. Nat. Neurosci 16, 264–266. 10.1038/nn.3329. [PubMed: 23396101]

Author Manuscript Author Manuscript Author Manuscript Author Manuscript

Highlights

- PFC regulates dorsal hippocampus (dHPC) via long-range GABAergic (LRG) projections
- LRG projections augment feedforward inhibition by targeting VIP interneurons in CA1
- PFC–dHPC LRG projections enhance object-related spatial encoding in CA1
- PFC–dHPC LRG projections promote object exploration and CA1-PFC gamma synchrony

Author Manuscript Author Manuscript Author Manuscript Author Manuscript

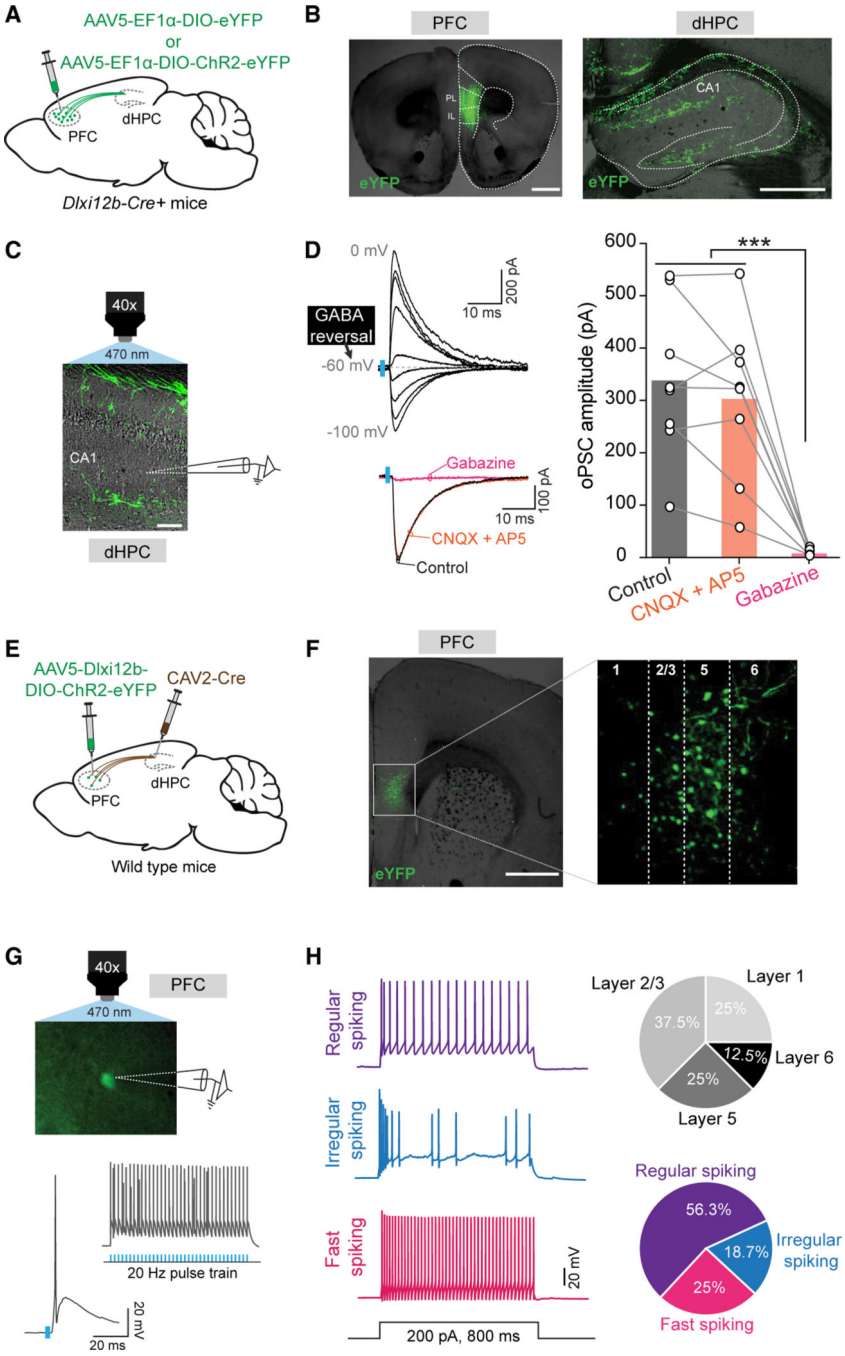

Figure 1. A heterogeneous population of PFC GABAergic neurons projects to the dHPC

(A) Schematic of the anterograde tracing strategy.

(B) Representative images of eYFP+ PFC GABAergic neurons (left) and eYFP+ axonal fibers in the dHPC (right). Scale bars, 1 mm and 0.5 mm, respectively.

(C) During patch clamp recordings from dorsal CA1 neurons, ChR2-eYFP+ LRG axon fibers (green) were optogenetically activated by blue light. Scale bar, 100 μm.

(D) Top left: example traces showing that optogenetically evoked postsynaptic currents (oPSCs) in CA1 neurons reverse at the GABA reversal potential (gray dashed line). Blue

Author Manuscript Author Manuscript Author Manuscript Author Manuscript

bars denote light pulses. Bottom left: example oPSCs recorded in control aCSF (black), after adding CNQX + AP5 (orange), and after adding Gabazine (magenta). Right: oPSC amplitudes were significantly reduced by Gabazine. Open circles represent data from individual neurons (n = 8) and bars represent averages; one-way ANOVA followed by Tukey's multiple comparison test, ***$p < 0.001$.

(E) Schematic of the intersectional strategy to label dHPC-projecting PFC LRG neurons.

(F) Representative images showing ChR2-eYFP-expressing, dHPC-projecting PFC LRG neurons. Dotted box (left) corresponds to magnified image (right). Numbers indicate the cortical layers. Scale bar, 1 mm.

(G) Top: representative image illustrating *ex vivo* patch clamp recording from ChR2-eYFP+ PFC– dHPC LRG neuron. Bottom: example traces showing PFC–dHPC LRG neuron firing elicited by a single light pulse or a 20 Hz train.

(H) Left: example voltage responses of PFC–dHPC LRG neurons to depolarizing current injections. Top right: pie chart showing the laminar distribution of recorded PFC–dHPC LRG neurons. Bottom right: pie chart showing percentages of PFC–dHPC LRG neurons with various physiological properties.

See also Figures S1 and S2 and Tables S1 and S2.

Author Manuscript Author Manuscript Author Manuscript Author Manuscript

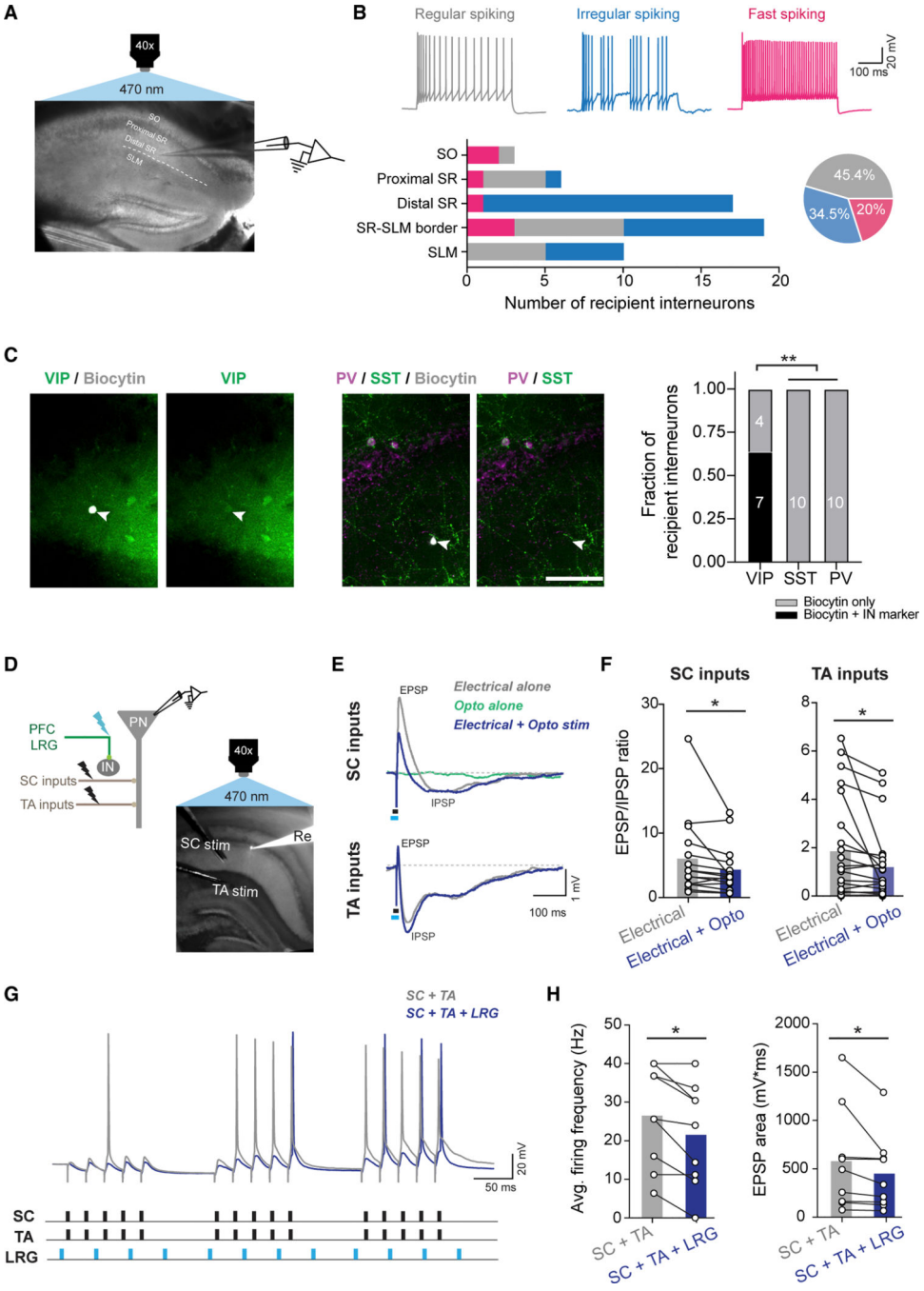

Figure 2. PFC LRG projections preferentially target ISIs and increase feedforward inhibition in CA1

(A) Example DIC image showing patch clamp recording from a CA1 neuron during optogenetic stimulation of PFC LRG projections. Layers of CA1 are labeled: stratum oriens (SO), stratum radiatum (SR), and stratum lacunosum-pyramidale (SLM); dashed white line represents the SR-SLM border.

(B) Top: example voltage responses to depolarizing current injections in recipient CA1 neurons. Bottom: laminar distribution (left) and % (right) of fast spiking (11/55), regular spiking (25/55), and irregular spiking (19/55) recipient CA1 neurons.

Author Manuscript Author Manuscript Author Manuscript Author Manuscript

(C) Left: Representative images showing IN marker expression in biocytin-filled recipient CA1 neurons. Scale bar, 100 μm. Right: fraction of recipient neurons that stained positive for VIP or (in separate sections) for PV or SST. Chi-square test, **$p < 0.01$.
(D) Top left: Schematic of the experimental configuration. Right: example hippocampal image showing Alexa-594 filled recording electrode (Re) targeting a CA1 PN, and electrodes for SC and TA stimulation. Brief pulses of blue light were used to optogenetically stimulate PFC LRG projections.
(E) EPSPs and IPSPs elicited by electrical stimulation of SC or TA inputs (black bar) in the presence or absence of optogenetic stimulation of PFC–dHPC LRG projections (cyan bar).
(F) Right: optogenetic stimulation of PFC–dHPC LRG projections significantly decreased EPSP/IPSP ratios for both SC (n = 15 cells) and TA (n = 22 cells) inputs. Open circles represent individual neurons and bars represent averages; two-way paired t test, *$p < 0.05$.
(G) Example voltage responses of a CA1 PN to coincident theta-burst stimulation (TBS) of SC and TA inputs (black bars) combined with 20 Hz optogenetic stimulation of PFC LRG projections (cyan bars).
(H) Average firing frequency (left) and EPSP area (right) during TBS of SC and TA inputs are reduced by concomitant optogenetic stimulation of PFC LRG projections. Open circles represent individual neurons (n = 9), and bars represent averages; two-way paired t test, *$p < 0.05$.
See also Figure S3 and Table S3.

Author Manuscript Author Manuscript Author Manuscript Author Manuscript

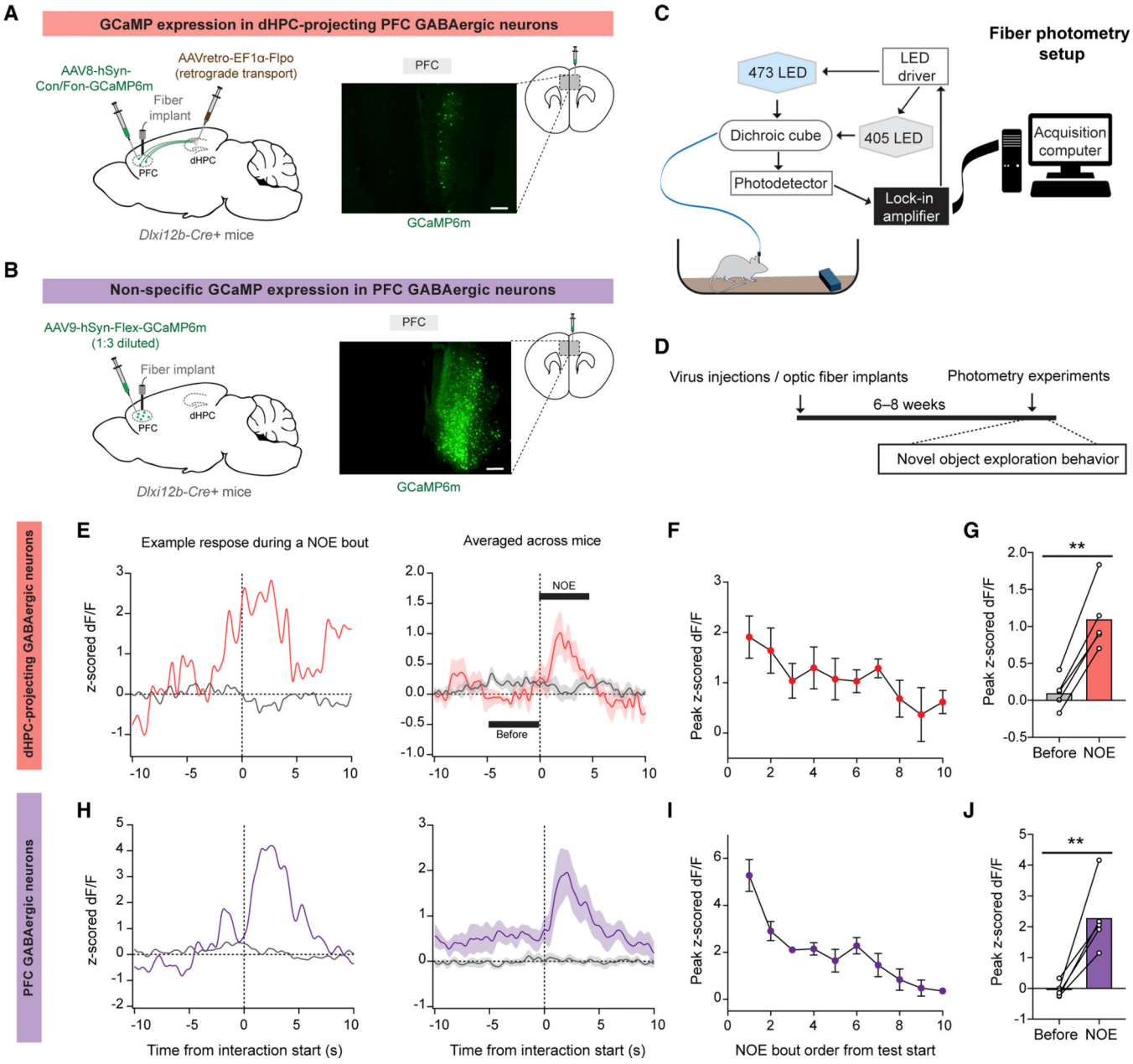

Figure 3. Activity of prefrontal GABAergic neurons is time-locked to NOE

(A) Left: Schematic of the intersectional strategy to specifically express GCaMP6m in dHPC-projecting PFC LRG neurons. Right: representative image showing sparse GCaMP expression in the cell bodies of PFC–dHPC LRG neurons. Scale bar, 200 μm.

(B) Similar to (A), for broad, non-specific GCaMP labeling of prefrontal GABAergic neurons. (C and D) Schematics of fiber photometry setup (C) and experimental design (D).

(C) Left: example trace showing NOE related changes in activity (z-scored dF/F) of dHPC-projecting PFC LRG neurons. Vertical dashed line indicates the start of NOE interaction bout. Right: averaged activity during NOE (n = 5 mice).

(D) Peak GCaMP6m z-scored dF/F of LRG neurons during multiple interaction bouts with a novel object.

Author Manuscript Author Manuscript Author Manuscript Author Manuscript

(E) Comparison of averaged z-scored dF/F before and after NOE bout start. Two-way paired t test, **p < 0.01.

(H–J) Same as (E)–(G) for non-specifically labeled prefrontal GABAergic neurons (n = 5 mice).

See also Figure S4.

Author Manuscript Author Manuscript Author Manuscript Author Manuscript

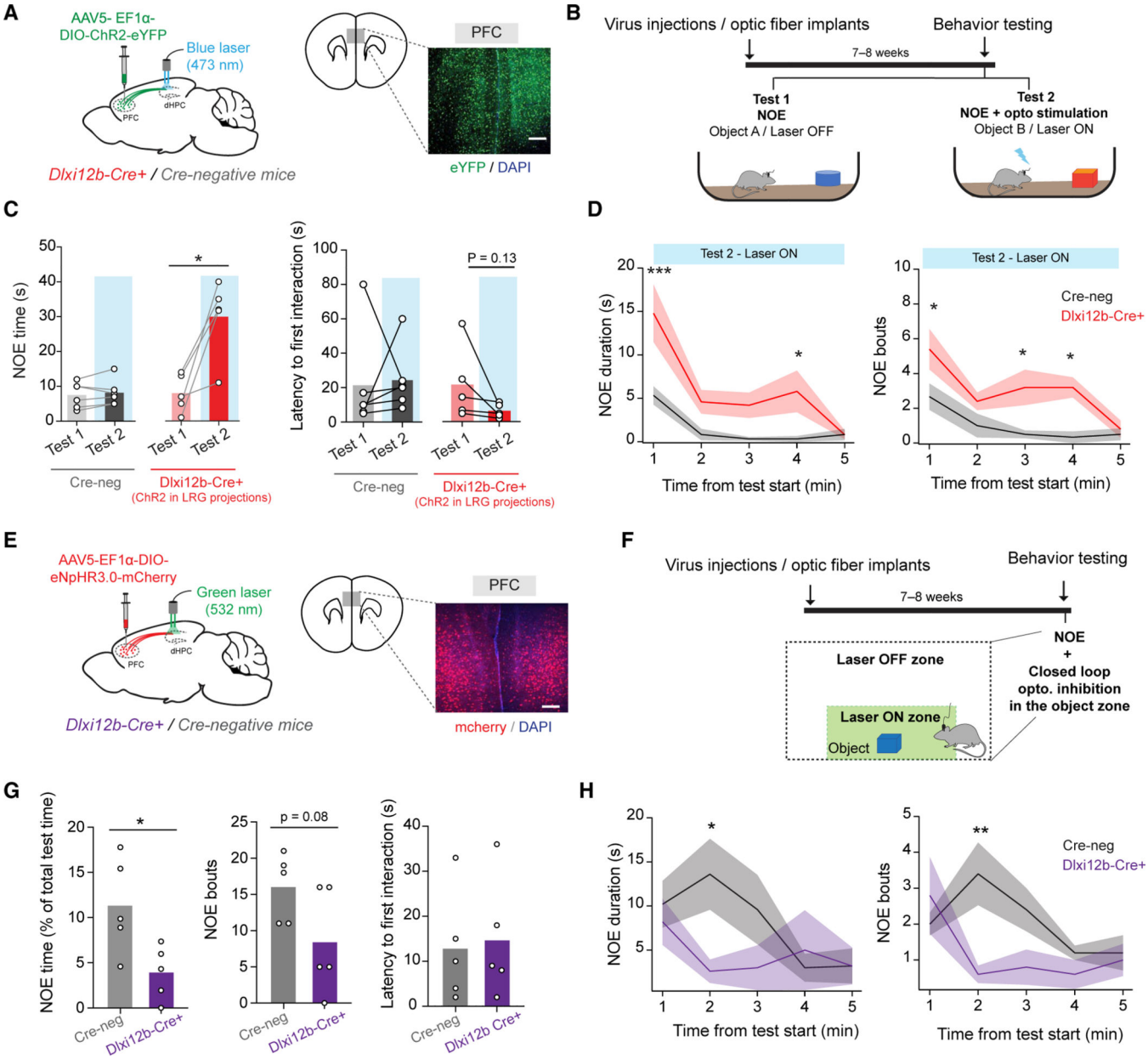

Figure 4. *In vivo* activity of PFC–dHPC LRG projections regulates NOE

(A) Left: schematic of the strategy for *in vivo* optogenetic stimulation. Right: representative image showing ChR2-eYFP expression in PFC GABAergic neurons. Scale bar, 200 μm.

(B) Experimental design: NOE was measured in the absence (Laser OFF, Test 1) or presence of optogenetic stimulation of LRG projections (Laser ON, Test 2).

(C) Left: optogenetic stimulation significantly increased NOE time in *Dlxi12b-Cre+* mice (n = 5) but not control mice (n = 6). Right: latency to first interaction with a novel object for *Cre+* and control mice is plotted. Open circles represent values from individual mice and bars indicate averages. Two-way paired t test, *p < 0.05.

Author Manuscript Author Manuscript Author Manuscript Author Manuscript

(D) Duration of NOE and number of NOE bouts within 1-min bins over the duration of a 5-min testing session. Solid lines represent averages, and shaded areas indicate SEM. Two-way repeated measures ANOVA, ***p < 0.001; *p < 0.05.

(E) Left: schematic showing the strategy for *in vivo* optogenetic inhibition. Right: representative image showing eNpHR3.0-mcherry expression in PFC GABAergic neurons. Scale bar, 200 μm.

(F) Experimental design for closed-loop optogenetic inhibition during NOE.

(G) Left: optogenetic inhibition of PFC–dHPC LRG projections significantly reduced NOE time in *Dlxi12b-Cre*+ mice (n = 5) but not controls (n = 5). Middle: number of NOE bouts for *Cre*+ and control mice. Right: latency to first interaction with the novel object. Open circles represent values from individual mice and bars indicate averages. Two-way unpaired t test, *p < 0.05.

(H) Duration of NOE and number of NOE bouts within 1-min bins during the first 5-min of testing session. Solid lines represent averages, and shaded areas indicate SEM. Two-way repeated measures ANOVA, **p < 0.01; *p < 0.05.

See also Figures S4 and S5.

Author Manuscript Author Manuscript Author Manuscript Author Manuscript

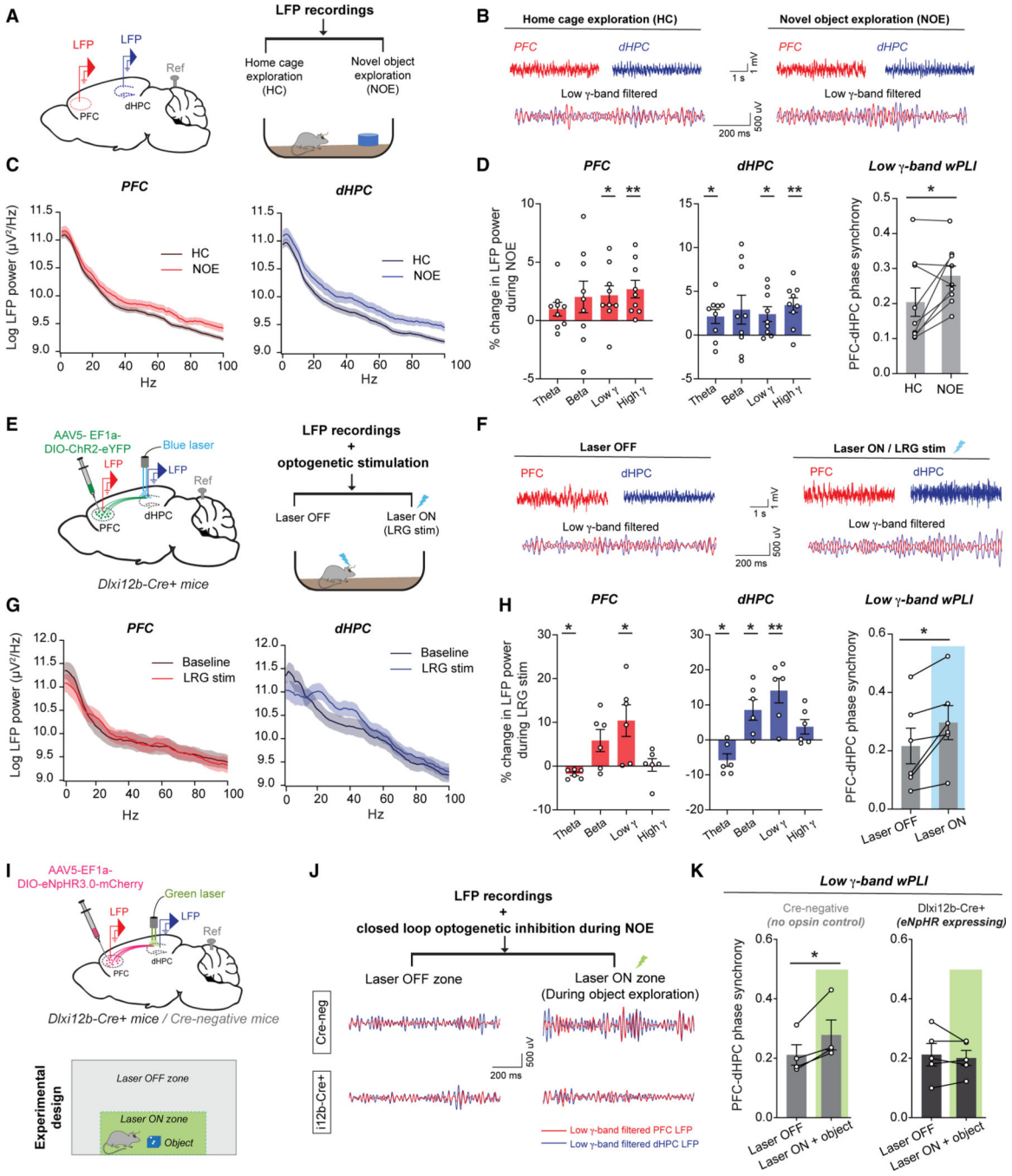

Figure 5. LRG projections regulate low-gamma (γ) oscillatory synchrony between the PFC and dHPC during NOE

(A) Left: LFP electrodes were implanted in PFC and dHPC; reference electrode was implanted over the cerebellum. Right: LFPs were recorded in home cage (HC) and during NOE.

(B) Example raw and low-γ frequency filtered LFPs recorded during HC and NOE epochs.

(C) Power spectrum of PFC and dHPC LFPs during HC and NOE. Solid lines represent the averages and shaded areas indicate SEM.

Author Manuscript Author Manuscript Author Manuscript Author Manuscript

(D) Left: % change in PFC and dHPC LFP log-power during NOE. Right: low-γ phase synchrony quantified using the weighted phase lag index (wPLI) between PFC and dHPC LFPs. Open circles represent data from individual mice (n = 9), and bars represent averages (± SEM). One-sample t test (LFP power) and two-way paired t test (phase synchrony), **p < 0.01; *p < 0.05.

(E) Schematic of the design for combined optogenetic stimulation and LFP recordings.

(F–H) Similar to (B)–(D) but for Laser OFF and Laser ON epochs (n = 6).

(I) Top: schematic of the design for combined optogenetic inhibition and LFP recordings. Bottom: During NOE behavior, LFPs recorded when mice explored an object in the Laser ON zone were compared to LFPs in the Laser OFF zone.

(J) Example low-γ band filtered PFC and dHPC LFPs recorded in the Laser ON (during object exploration) and Laser OFF zones.

(K) Comparison of PFC-dHPC low-γ phase synchrony in the Laser OFF and Laser ON zones. Object exploration was associated with significantly higher low-γ synchrony in controls (n = 4) but not eNpHR-expressing *Cre*+ mice (n = 5). Open circles represent data from individual mice, and bars represent averages (± SEM). Two-way ANOVA followed by Bonferroni's multiple comparisons test, *p < 0.05. See also Table S4.

Author Manuscript Author Manuscript Author Manuscript Author Manuscript

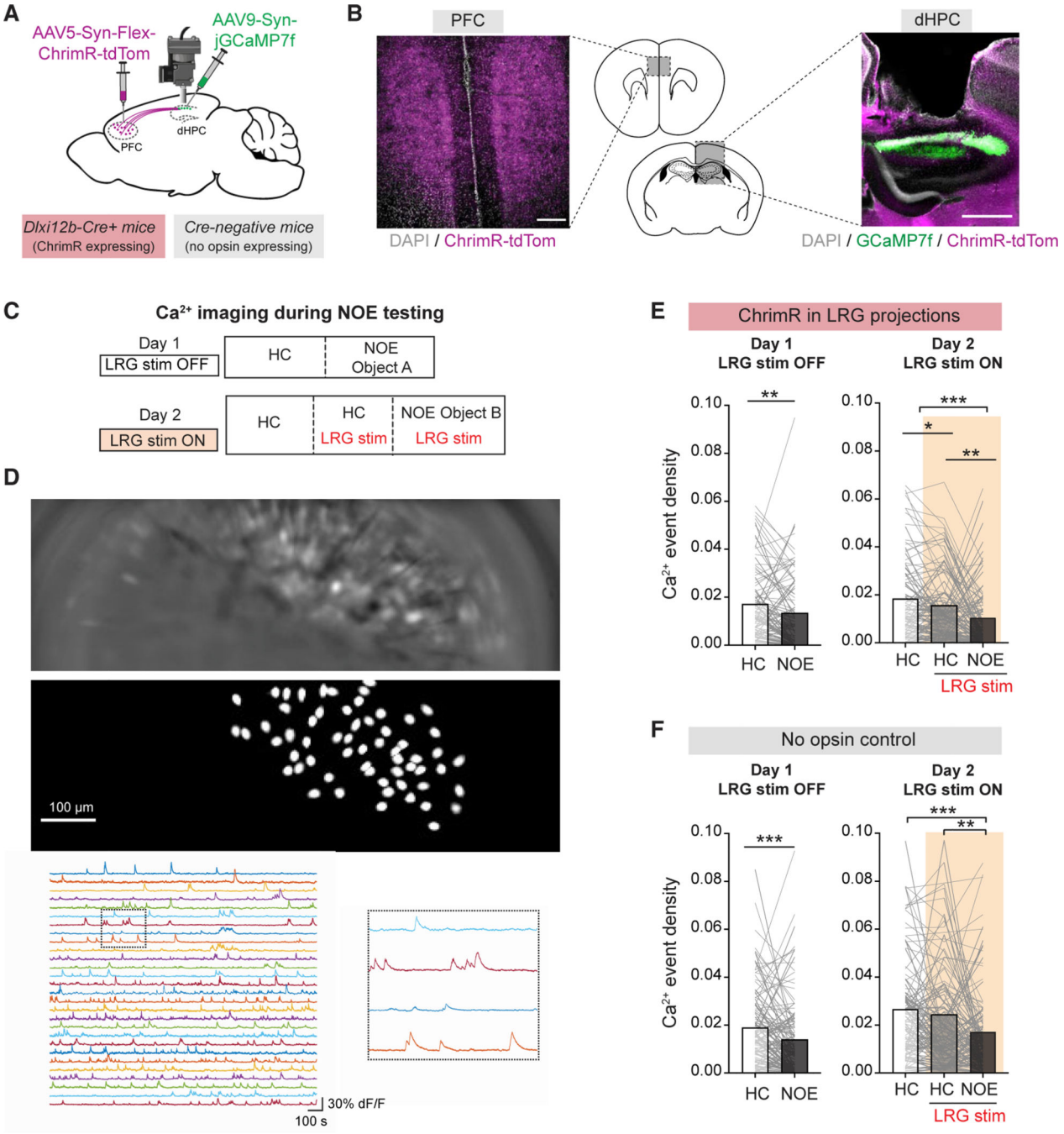

Figure 6. PFC–dHPC LRG projections shape CA1 neuronal activity during object exploration

(A) Strategy for *in vivo* Ca^{2+} imaging and optogenetic stimulation.

(B) Left: Example image showing ChrimR-tdTom expression in PFC GABAergic neurons. Right: Example of jGCaMP7f expression in CA1 neurons and ChrimR-tdTom expression in PFC–dHPC LRG axonal fibers. Scale bars, 250 µm (left) and 500 µm (right).

(C) Experimental design. Day 1: CA1 Ca^{2+} activity was measured during home cage (HC) and NOE epochs. Day 2: after initial imaging in HC without optogenetic stimulation, Ca^{2+}

Author Manuscript Author Manuscript Author Manuscript Author Manuscript

imaging was combined with optogenetic stimulation of PFC–dHPC LRG projections during HC and NOE epochs.

(D) Top: FOV and ROIs (corresponding to neurons) from a representative Ca^{2+} imaging session. Bottom: example extracted dF/F Ca^{2+} transients.

(E) Left: activity of CA1 neurons was significantly reduced during NOE. Each gray line represents a single neuron and bars represent the means (n = 97 neurons from 3 mice); Wilcoxon rank-sum test. Right: During the HC epoch on day 2, optogenetic stimulation of PFC–dHPC LRG projections reduced CA1 Ca^{2+} activity. On day 2, activity was then further reduced during NOE (n = 108 neurons, 3 mice). Friedman test followed by Dunn's multiple comparison test; ***p < 0.001, **p < 0.01, *p < 0.05.

(F) Same as E for opsin-negative controls. Activity of CA1 neurons was significantly reduced during NOE. Note, light delivery alone did not affect Ca^{2+} activity (day 1: n = 119 neurons, 4 mice; day 2: n = 118 neurons, 4 mice). ***p < 0.001, **p < 0.01.

See also Figure S6.

Author Manuscript Author Manuscript Author Manuscript Author Manuscript

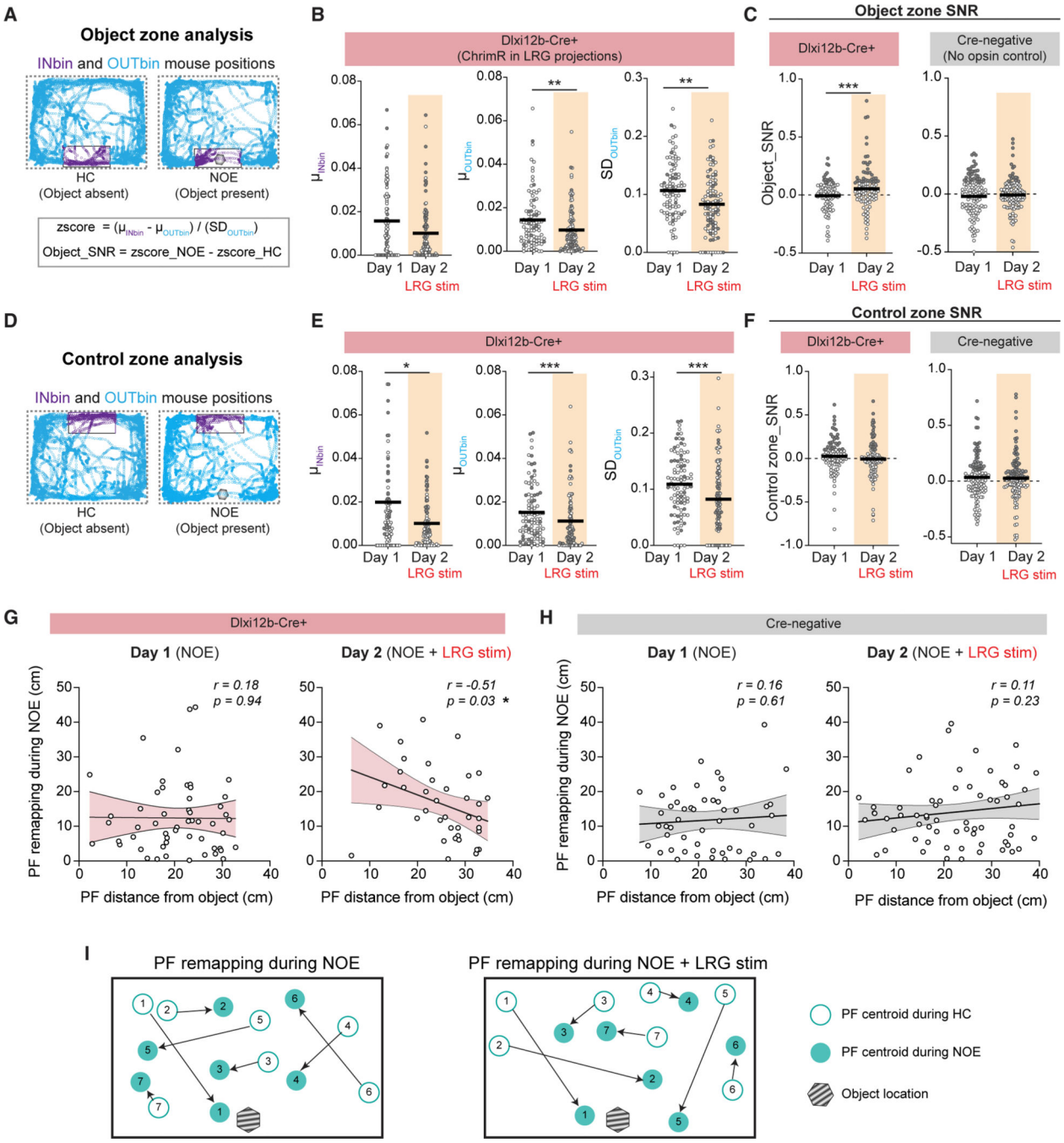

Figure 7. PFC–dHPC LRG projections increase signal-to-noise ratio for CA1 encoding of object locations

(A) Top: Mouse positions during HC (left) and NOE (right) epochs from example day 2 recording session. Blue circles indicate frames where mouse was outside the object zone ("OUTbin"). Purple circles indicate frames where mouse was in the object zone ("INbin"). Gray hexagon = novel object location during NOE epoch. Black rectangle = object zone. Bottom: z-scored activity = difference between Ca^{2+} activity within (μ_{INbin}) vs. outside (μ_{OUTbin}) object zone, divided by standard deviation of activity outside object zone (SD_{OUTbin}). Object_SNR = difference in z-scored activity between HC and NOE.

Author Manuscript Author Manuscript Author Manuscript Author Manuscript

(B) μ_{INbin}, μ_{OUTbin}, and SD_{OUTbin} values for CA1 neurons on day 1 (NOE) and day 2 (NOE + LRG stim). Two-way unpaired t test; **p < 0.01.

(C) Object_SNR was increased on day 2 compared to day 1 in ChrimR-expressing mice (left) but not opsin-negative controls (right). Empty gray circles represent individual neurons and horizontal black lines show means. Filled gray circles indicate neurons exceeding an arbitrary threshold for Object_SNR (>0.1). Two-way unpaired t test; ***p < 0.001.

(D) Same as (A) for analysis of a control zone (not containing an object).

(E) Similar to (B), showing μ_{INbin}, μ_{OUTbin}, and SD_{OUTbin} based on the control zone. ***p < 0.001, *p < 0.05.

(F) Similar to (C), SNR calculated based on a control zone. Unlike Object_SNR, control zone_SNR was not affected by stimulating LRG projections.

(G) Left: On day 1, place field (PF) remapping distance during NOE was not correlated with the PF distance from the object in *Dlxi12b-Cre*+ mice. Right: during NOE + LRG stim on day 2, PF remapping distance during NOE was significantly correlated with the PF distance from the object. Open circles indicate individual place cells, solid lines indicate regression lines, and shaded regions indicate 95% confidence intervals. *p < 0.05.

(H) Same as (G), for Cre-negative controls.

(I) Cartoon of PF remapping. Open circles indicate PF centroids during HC. Filled circles indicate PF centroids during NOE. Hexagon indicates object. Arrows indicate remapping distance.

See also Figures S6 and S7 and Tables S5–S7.

Author Manuscript Author Manuscript Author Manuscript Author Manuscript

Cell. Author manuscript; available in PMC 2023 March 20.

KEY RESOURCES TABLE

REAGENT or RESOURCE	SOURCE	IDENTIFIER
Antibodies		
Rabbit anti-Parvalbumin antibody	Swant	PV27; RRID: AB_2631173
Rat anti-Somatostatin antibody	Millipore Sigma	MAB354; RRID: AB_2255365
Rabbit anti-VIP antibody	Immunostar	20077; RRID: AB_1073072
Alexa Flour 594 Cholera toxin beta subunit conjugate (CTb-594)	Invitrogen	C34777
Rabbit anti-Calretinin antibody	Immunostar	24445; RRID: AB_572223
Goat anti-CTb antibody	List labs	703, RRID: AB_10013220
Rabbit anti-nNOS antibody	Thermo Fisher	61–7000; RRID: AB_2313734
Rabbit anti-NPY antibody	Immunostar	24506; RRID: AB_572257
Streptavidin Alexa-647 conjugate	Thermo Fisher	S21374; RRID: AB_2336066
Donkey anti-rabbit Alexa-488 antibody	Thermo Fisher	A32790; RRID: AB_2762833
Donkey anti-rat Alexa 594 antibody	Thermo Fisher	A21209; RRID: AB_2535795
Donkey anti-rat Alexa 488 antibody	Thermo Fisher	A21208; RRID: AB_2535794
Donkey anti-goat Alexa 594 antibody	Thermo Fisher	A32758; RRID: AB_2762828
Bacterial and virus strains		
AAV5-EF1α-DIO-ChR2-eYFP	UNC Vector Core	N/A
AAV5-EF1α-DIO-eYFP	UNC Vector Core	N/A
AAV5-EF1α-eNpHR3.0-mcherry	UNC Vector Core	N/A
AAVretrograde-EF1a-Flpo	Addgene	Addgene viral prep # 55637-AAVrg
AAV8-CON/FON-GCaMP6m	Addgene	Addgene viral prep # 137119-AAV8
AAV8-CON/FON-eYFP	Addgene	Addgene viral prep # 55650-AAV8
AAV5-Syn-FLEX-ChrimsonR-tdTomato	Addgene	Addgene viral prep # 62723-AAV5
AAV9-Syn-jGCaMP7f-WPRE	Addgene	Addgene viral prep # 104488-AAV9
CAV2-Cre	CNRS BioCampus	N/A
AAV9-Syn-flex-GCaMP6m-WPRE	Addgene	Addgene viral prep # 100838-AAV9
Chemicals, peptides, and recombinant proteins		

Author Manuscript
Author Manuscript
Author Manuscript
Author Manuscript

REAGENT or RESOURCE	SOURCE	IDENTIFIER
Gabazine	Tocris	Cat # 1262
CNQX	Tocris	Cat # 0190
AP5	Tocris	Cat # 0106
Experimental models: Organisms/strains		
PV-Cre	The Jackson Laboratory	RRID: IMSR_JAX:008069
SST-IRES-Cre	The Jackson Laboratory	RRID: IMSR_JAX:013044
VIP-Cre	The Jackson Laboratory	RRID: IMSR_JAX:010908
Software and algorithms		
MATLAB	Mathworks	RRID: SCR_001622; v2017a
IGOR Pro	Wavemetrics	RRID: SCR_000325; v7
Image-J software	ImageJ	https://imagej.nih.gov/ij/
Prism 9	Graphpad	RRID:SCR_002798
pCLAMP 10	Molecular Devices	RRID:SCR_011323
ClampFit 10.5	Molecular Devices	N/A
ANY-maze behavioral tracking software	Stoelting Co.	https://www.any-maze.com/
Sirenia software	Pinnacle Technology Inc	https://www.pinnaclet.com/sirenia.html
nVoke	Inscopix	N/A
Inscopix Data Processing software	Inscopix	N/A
Analysis Code	This paper	https://github.com/ruchimalik/malik_etal_cell2022